uOttawa

L'Université canadienne
Canada's university

**FACULTÉ DES ÉTUDES SUPÉRIEURES ET POSTOCTORALES**

uOttawa

L'Université canadienne
Canada's university

**FACULTY OF GRADUATE AND POSDOCTORAL STUDIES**

Adrian Pegoraro
AUTEUR DE LA THÈSE / AUTHOR OF THESIS

M.Sc. (Physics)
GRADE / DEGREE

Department of Physics
FACULTÉ, ÉCOLE, DÉPARTEMENT / FACULTY, SCHOOL, DEPARTMENT

Modelling Heterogeneous Nonlinear Subwavelength Systems with the Finite Difference Time Domain Method
TITRE DE LA THÈSE / TITLE OF THESIS

T. Brabec
DIRECTEUR (DIRECTRICE) DE LA THÈSE / THESIS SUPERVISOR

CO-DIRECTEUR (CO-DIRECTRICE) DE LA THÈSE / THESIS CO-SUPERVISOR

EXAMINATEURS (EXAMINATRICES) DE LA THÈSE / THESIS EXAMINERS

| | |
|---|---|
| J. Armitage | R. Bhardwaj |
| L. Chen | |
| | |

Gary W. Slater
LE DOYEN DE LA FACULTÉ DES ÉTUDES SUPÉRIEURES ET POSTDOCTORALES /
DEAN OF THE FACULTY OF GRADUATE AND POSTDOCORAL STUDIES

# Modelling Heterogeneous Nonlinear Subwavelength Systems with the Finite Difference Time Domain Method

Adrian Pegoraro

Thesis submitted to the
Faculty of and Graduate and Postdoctoral Studies
In partial fulfillment of the requirements
For the M. Sc. Degree in Physics

Physics
Science
University of Ottawa

© Adrian Pegoraro, Ottawa, Canada, 2005

Library and
Archives Canada

Published Heritage
Branch

395 Wellington Street
Ottawa ON K1A 0N4
Canada

Bibliothèque et
Archives Canada

Direction du
Patrimoine de l'édition

395, rue Wellington
Ottawa ON K1A 0N4
Canada

*Your file Votre référence*
*ISBN: 0-494-11379-0*
*Our file Notre référence*
*ISBN: 0-494-11379-0*

NOTICE:
The author has granted a non-exclusive license allowing Library and Archives Canada to reproduce, publish, archive, preserve, conserve, communicate to the public by telecommunication or on the Internet, loan, distribute and sell theses worldwide, for commercial or non-commercial purposes, in microform, paper, electronic and/or any other formats.

The author retains copyright ownership and moral rights in this thesis. Neither the thesis nor substantial extracts from it may be printed or otherwise reproduced without the author's permission.

AVIS:
L'auteur a accordé une licence non exclusive permettant à la Bibliothèque et Archives Canada de reproduire, publier, archiver, sauvegarder, conserver, transmettre au public par télécommunication ou par l'Internet, prêter, distribuer et vendre des thèses partout dans le monde, à des fins commerciales ou autres, sur support microforme, papier, électronique et/ou autres formats.

L'auteur conserve la propriété du droit d'auteur et des droits moraux qui protège cette thèse. Ni la thèse ni des extraits substantiels de celle-ci ne doivent être imprimés ou autrement reproduits sans son autorisation.

---

In compliance with the Canadian Privacy Act some supporting forms may have been removed from this thesis.

While these forms may be included in the document page count, their removal does not represent any loss of content from the thesis.

Conformément à la loi canadienne sur la protection de la vie privée, quelques formulaires secondaires ont été enlevés de cette thèse.

Bien que ces formulaires aient inclus dans la pagination, il n'y aura aucun contenu manquant.

Canada

# Table of Contents

# List of Figures

# Acknowledgements

Coming from an engineering physics background to work in modeling nonlinear optics, I faced a steep learning curve, but had many people to help me achieve my goal. Dr. Thomas Brabec was an excellent supervisor and teacher. He was always available to answer any questions I might have and offered guidance on how to best approach the problems I encountered Dr. Lora Ramunno, a post-doc in the group, provided invaluable assistance while I was getting started. It was her code which I modified to create the final version which was used for all experiments. Dr. Andy Risdale provided an interesting problem to test our model and was helpful in explaining the experiments and methods used. The figures in section 3.1 were provided by Dr. Risdale. Dr. Albert Stolow initially advised me to seek out Thomas and continued to offer me advice and assistance during my time with Thomas. Dr. Christian Jungreuthmayer provided answers to any technical questions I had and continued to assist even after he finished his Ph. D. Chris McDonald took over technical maintenance after Christian left, and has been of assistance whenever possible. Dr. Zhongxi Zhang, Dr. Alexander Pegarkov and Dr. Carlos DeStefani have been a pleasure to work with in the lab.

Finally, I would like to thank my parents, Liz and Frank Pegoraro, my sister Oriana Pegoraro and my girlfriend Tracy Wong for their support and encouragement. Their patience, advice and support have been invaluable and I would not have been able to achieve what I have without it.

# Abstract

Predicting the response of heterogeneous nonlinear microscopic systems to laser excitation is very difficult using analytical techniques and is only feasible under simplifying assumptions. However, using numerical methods, it is possible to analyze arbitrary systems and make predictions about their behaviour. This information may be used to develop new techniques and a better understanding of measurements. One area which stands to benefit from such methods is nonlinear microscopy. We use finite difference time domain methods to explain experimental measurements and also develop a new nonlinear microscopy technique which shows a significant improvement in axial resolution over traditional techniques. We then explore the behaviour of Maxwell Garnett nanocomposites and illustrate the limitations of the current theoretical models for these systems.

# 1 Introduction

Since the invention of the microscope, people have worked towards achieving imaging with high lateral spatial resolution, 3-D sectioning capability and high contrast in order to characterize specimens. This drive has led to the evolution of many different types of linear microscopy. Fluorescence confocal microscopy achieves these three goals; however, it often requires the addition of exogenous fluorophores for imaging biological systems. Some dyes and fluorescent labels disturb the natural evolution of a biological system, ruining any observations made or killing the specimen outright. Also, using fluorescent microscopy, the fluorophores may be bleached which often leads to cell damage. Raman microscopy and infrared imaging achieve contrast through probing the vibrational modes of the molecules in order to achieve chemical selectivity. Unfortunately infrared imaging achieves a poor resolution because of the long wavelengths used. As for Raman imaging, it normally exhibits a very weak signal (most molecules have a small Raman cross section) which necessitates slow measurements or high laser intensities. High intensities create a large background auto-fluorescence signal that reduces contrast. A more fundamental limit of linear microscopy is that the spatial resolution cannot exceed the diffraction limit of light. Because of this, the only way to improve resolution is to use shorter wavelengths. In many biological systems, these frequencies of light (i.e. UV) are absorbed or generate a large background signal and hence are not practical for imaging. These limitations may be overcome using nonlinear optical processes in combination with linear microscopy.

One of the key advantages of nonlinear microscopy is an enhanced spatial resolution. Nonlinear processes rely on high intensities in order to generate appreciable signal. These high intensities can be generated using tight focussing of the incoming light using high numerical aperture (NA) lenses. The effective excitation volume generating the nonlinear signal will be smaller than that of a linear signal because of the requirement for high intensity (smaller by a factor of $\sqrt{2}$ [1] for second order processes and $\sqrt{3}$ [1] for third order ones). Furthermore, since the signal is generated only from the focal volume, this provides a natural way to achieve three dimensional sectioning without the need for confocal geometry.

A second advantage of nonlinear microscopy is that the excitation wavelength can be longer than in linear microscopy. While making use of this somewhat offsets the advantage of the enhanced spatial resolution, it offers several distinct advantages if one is examining condensed media. By using near-infrared light, it is possible to avoid absorption of the excitation pulses in the solvent which allows imaging of specimens embedded in condensed matter. This property is necessary for imaging live cells *in vivo* and imaging tissue is not possible without it.

A third advantage is the ability to achieve chemical specificity without the addition of exogenous fluorophores. This is possible by making use of resonant energy levels in the molecules of interest to greatly enhance the desired output signal. By avoiding the use of fluorescent tags, this allows for the *in vivo* or *in vitro* study of live cells without disturbance of natural cellular processes. Not all types of nonlinear microscopy have this feature (second and third harmonic generation and multiphoton fluorescence do not), but others do (sum frequency generation and coherent anti-Stokes Raman scattering).

A final advantage is the low average power necessary if one employs ultrafast laser pulses. The field of ultrafast lasers is now mature and devices are now available which are tuneable over a wide frequency range, making it possible to generate large nonlinear signals while using a low average power. This eliminates the problem of cell damage that can occur when dealing with linear microscopy (and associated bleaching effects). Also, with less energy deposited into the sample, the overall system suffers less negative effects due to the excitation (e.g. heating).

All of these advantages are available with coherent anti-Stokes Raman scattering (CARS) microscopy [1]. This is a third order process in which vibrational levels of a molecule are excited. This offers the possibility of functional imaging, i.e. imaging specific chemical groups and following them inside the sample. Using such techniques, it should be possible to watch viral RNA invade a cell and then use this information to help identify means of blocking infection. However, before this goal can be achieved, it is necessary to improve the resolution and contrast beyond what is currently possible with this technique.

One method of study which allows us to look for improvements is using calculations of nonlinear signal generation in a model cell. The small length scale (most objects are on the nanometer scale) and natural heterogeneity of a cell make most methods of study prohibitively difficult or require many simplifications. However, using finite difference time domain (FDTD) [2-4] techniques, it is possible to perform *ab initio* calculations of signal generation while defining a structure that is arbitrarily complicated.

This type of model, however, need not be limited only to microscopy applications. By being able to choose an arbitrarily shaped medium with each part exhibiting a chosen nonlinearity, it is possible to study scattering from objects randomly embedded in a host medium. Using the FDTD model developed, it is possible to choose any arrangement of scatterers and look for possible enhancements (or reductions) of the nonlinear signal generated by the composite medium. This information can be applied to microscopy as well as other fields (for example, nonlinear signal generation in fibers). For microscopy, this opens the possibility of understanding signal generation from heterogeneous systems. For nonlinear optical fibers, if it can be shown that there is an enhancement of the nonlinear susceptibility through addition of a scattering media, this may allow for the design and fabrication of new, more efficient fibers.

One such scheme which has been proposed to generate an enhancement of nonlinear susceptibility is a Maxwell Garnett nanocomposite [5]. These nanocomposites are formed by randomly placing small spherical inclusions inside a host medium with both the inclusions and the host exhibiting nonlinearity. However, such a medium is very complex and may only be solved analytically using simplifying assumptions. It is difficult to correlate these predictions to experiments since these assumptions are difficult to maintain in practice. However, using FDTD methods, it is possible to design a realistic nanocomposite and investigate the change in nonlinear susceptibility that occurs. Also it is possible to better understand the region of applicability of the current models and where improvements are most needed.

The outline of this thesis is as follows. The FDTD model is introduced in section 2. This covers the equations used and their implementation. It also discusses some of the limitations with the current model. Section 3 deals with a possible new type of microscopy using the optical Kerr effect. This problem was brought to us by a collaborator in the hopes our FDTD model could explain some anomalous measurements. A CARS microscopy scheme is introduced in section 4 which offers significant improvements in the axial resolution possible with CARS microscopy (up to 40 times better than what has previously been demonstrated). The FDTD model is used to confirm the expected improvements. Section 5 deals with Maxwell Garnett nanocomposites and studying the change of the nonlinear susceptibility when the inclusions are densely packed. This regime cannot be addressed by any strict analytic arguments and may only be investigated using numerical techniques such as FDTD. It is found the current models overestimate the enhancement of nonlinear susceptibility, especially as the density of scatterers increases. The conclusion and references follow section 5.

# 2 Finite Difference Time Domain Model

The finite difference time domain (FDTD) is a powerful numerical technique for solving Maxwell's equations. It was first introduced by Yee in 1966 [2] and has grown continuously ever since. The advantage of using FDTD is that, in principle, any object may be modelled in any electromagnetic interaction. In practice, computer processing speed and memory limit what can be modelled. However, standard implementations of FDTD are often highly parallelizable and new applications which were previously unfeasible can now be addressed with the rise of new supercomputing clusters which offer significantly more computing power than was previously commonly available. For our experiments, we studied heterogeneous nonlinear microscopic structures.

## *2.1 Model Development*

FDTD is used to model the electric and magnetic fields in system. The system is divided into many cells, and Maxwell's equations are solved point by point for each time step. The model used can be broken into several parts: the source, the boundaries and the propagating medium. The source and boundaries make use of standard FDTD techniques and have been well covered in literature [3, 4]. Briefly, we use either absorbing or periodic boundary conditions. The absorbing boundary conditions are used to represent an isolated object (scattered light exits the system and propagates to infinity). Periodic boundary conditions assume an identical system excited with identical incoming light exists adjacent to the system of interest (scattered light leaves one side of the system and simultaneously enters it from the opposite). The use of periodic boundary conditions can be used to move from 3-D to 2-D or 1-D simulations by eliminating the desired dimension by making it only one cell wide. For example, 2-D propagation in the xz plane may be modeled by making y one cell wide with periodic boundary conditions (in effect, y extends to infinity and is uniform).

The source used may be either a total-field, scattered-field (TFSF) source or a soft-source. TFSF defines two regions, the total field and the surrounding scattered field region. In the scattered region, the incoming excitation is subtracted so only light that has been scattered from the total field region exists. This allows for plane wave excitation without the incident pulse interacting with absorbing boundary conditions (which causes instability), while still allowing the light scattered by structures inside the medium is to escape to the absorbing boundary conditions and exit the system. The implementation of the TFSF technique has been described elsewhere [4]. A soft-source is when the electric field is specified at several points in the propagating medium. These points act like temporary point charges and the electric field will propagate away from the points. By choosing the correct location and phase relation, it is possible to specify any incoming pulse shape. This technique is used to introduce Gaussian pulses into the system. The absorbing boundary conditions do not interact with the source since the Gaussian pulse goes to zero before reaching the system boundaries, so stability is not an issue. One inconvenience of this implementation is that it requires that the system defined be large enough to encompass the entire pulse.

For propagation inside a nonlinear medium, there are several different approaches [4, 6-8] and we chose to follow [6]. We start with Maxwell's equations in a medium with no free charges (note, equations are in MKS units):

$$\frac{\partial \vec{D}}{\partial t} = \nabla \times \vec{H} \qquad \boxed{1}$$

$$\vec{D} = \vec{E} + \vec{P} \qquad \boxed{2}$$

$$\frac{\partial \vec{H}}{\partial t} = \frac{-1}{\mu_0} \nabla \times \vec{E} \qquad \boxed{3}$$

The standard FDTD notation is to represent each field in time with an upper index and the direction of the field with a lower index. The spatial coordinates of the field are given by the values in brackets. Equations (4) – (6) allow one to find each field in the x direction for the next time step. It should be noted, magnetic and electric fields are found at different space locations (staggered field approach), so they are found at different times as well (they are separated by half a space and time step). For our code, we made use of a three dimensional representation and similar equations were used for the y and z directions:

$$\frac{D_x^{n+0.5}(i,j,k)-D_x^{n-0.5}(i,j,k)}{\Delta t}=\frac{H_z^n(i,j+0.5,k)-H_z^n(i,j-0.5,k)}{\Delta y}-\frac{H_y^n(i+0.5,j,k)-H_y^n(i-0.5,j,k)}{\Delta x} \qquad \boxed{4}$$

$$E_x^{n+0.5}=D_x^{n+0.5}-P_x^{n+0.5} \qquad \boxed{5}$$

$$\frac{H_x^{n+1}(i,j,k)-H_x^{n-1}(i,j,k)}{\Delta t}=\frac{1}{\mu_0}\frac{E_y^{n+0.5}(i+1,j,k)-E_y^{n+0.5}(i,j,k)}{\Delta x}-\frac{1}{\mu_0}\frac{E_z^{n+0.5}(i,j+1,k)-E_z^{n+0.5}(i,j,k)}{\Delta y} \qquad \boxed{6}$$

Δt is one time step and Δx (or Δy) is one step in space (the Courant stability criteria is used, Δt = Δx/2/c). The superscript denotes the time step (i.e. time step n or n+0.5). In our code, all space dimensions are identical.

The polarization term in (5) can be expanded into several different linear and nonlinear terms. This presents a problem when attempting to determine stability criteria. When using linear FDTD, normally one requires the cell size be at maximum λ/10 [4]. This same criteria was used for our simulations, except it was required that the largest possible frequency be governed by this same restriction (dispersion limited the attainable frequencies to be reasonable). Looking at the linear portion of $P_x$, three Lorentz poles were used. Using these poles, it is possible to represent the index of refraction over a wide frequency range using the well known Sellmeier parameters [9]. Looking at the example of one pole, we see that it is possible to transform the equation from the frequency domain into the time domain.

$$\vec{P}_L(\omega)=\chi_L^{(1)}\vec{E}(\omega)=\frac{\varepsilon_0\varepsilon_L\omega_L^2}{\omega_L^2-2j\omega\delta_L-\omega^2} \qquad \boxed{7}$$

$$\omega_L^2\vec{P}_L(t)+2\delta_L\frac{\partial\vec{P}_L(t)}{\partial t}+\frac{\partial^2\vec{P}_L(t)}{\partial t^2}=\varepsilon_0\Delta\varepsilon_L\omega_L^2\vec{E}(t) \qquad \boxed{8}$$

where $\Delta\varepsilon_L$ is a scaling factor, $\omega_L$ is the pole frequency, and $\delta_L$ is the damping factor. The time domain equation can then be transformed into an FDTD form using central differencing for the time derivatives. Notice that we solve for the polarization, not the electric field.

$$P_L^{n+0.5} = a_L P_L^{n-0.5} + b_L P_L^{n-1.5} + c_L E^{n-0.5} \qquad \boxed{9}$$

$$a_L = \frac{2 - \omega_L^2 \Delta t^2}{1 + \delta_L \Delta t} \qquad \boxed{10}$$

$$b_L = \frac{\delta_L \Delta t - 1}{1 + \delta_L \Delta t} \qquad \boxed{11}$$

$$c_L = \frac{\varepsilon_0 \Delta\varepsilon_L \omega_L^2 \Delta t^2}{1 + \delta_L \Delta t} \qquad \boxed{12}$$

For our model, we included two Raman nonlinear terms and Kerr nonlinearity. The Raman nonlinearity can be modeled under the Born-Oppenheimer approximation [10] as:

$$P_R(t) = \varepsilon_0 E(t) \left[ \chi_0^{(3)}(t) * E^2(t) \right] \qquad \boxed{13}$$

$$\chi_0^{(3)} = \chi_R^{(3)} g_R(t) \qquad \boxed{14}$$

and we let

$$S(t) = \chi_0^{(3)} * E^2(t) \qquad \boxed{15}$$

where $*$ represents convolution and $g_R$ is the response function for the Raman nonlinearity. We now must solve for the auxiliary variable S(t). A Raman oscillator in an electric field may be thought of as a driven, damped harmonic oscillator [11]. This allows us to represent the Raman nonlinearity as a retarded response function in frequency space, and we can follow the same procedure as for the Lorentz poles.

$$\chi_0^{(3)}(\omega) = \frac{\chi_R^{(3)}}{\omega_R^2 + 2j\omega\delta_R - \omega^2} \qquad \boxed{16}$$

$$S^{n+0.5}=a_R S^{n-0.5}+b_R S^{n-1.5}+c_R(E^{n-0.5})^2 \qquad \boxed{17}$$

$$a_R=\frac{2-\omega_R^2\Delta t^2}{1+\delta_R\Delta t} \qquad \boxed{18}$$

$$b_R=\frac{\delta_R\Delta t-1}{1+\delta_R\Delta t} \qquad \boxed{19}$$

$$c_R=\frac{\chi_R^{(3)}\omega_R^2\Delta t^2}{1+\delta_R\Delta t} \qquad \boxed{20}$$

To represent the Kerr nonlinearity, we assume it is instantaneous and hence we find:

$$P_K(t)=\varepsilon_0\chi_k^{(3)}E(t)\int\delta(t-t')E^2(t')dt' \qquad \boxed{21}$$

$$P_K^{n+0.5}=\varepsilon_0\chi_K^{(3)}\left(E^{n+0.5}\right)^3 \qquad \boxed{22}$$

Combining all the polarization terms, we can now modify (5) where we take the sum over all Lorentz and Raman poles as well as include Kerr nonlinearity so that we have:

$$P^{n+0.5}=\sum P_L^{n+0.5}+\sum P_R^{n+0.5}+P_K^{n+0.5} \qquad \boxed{23}$$

where

$$P_R^{n+0.5}=\varepsilon_0 E^{n+0.5}S^{n+0.5} \qquad \boxed{24}$$

Substituting (23) into (5), we can solve for the electric field at the n+0.5 time step using the equation:

$$E^{n+0.5}=\frac{D^{n+0.5}-\sum P_L^{n+0.5}}{\varepsilon_0\left(\varepsilon_\infty+\sum S^{n+0.5}+\chi_K^{(3)}\left(E^{n+0.5}\right)^2\right)} \qquad \boxed{25}$$

Equation (25) must be iterated to solve for the electric field. Using the procedure outlined above, it is possible to find the magnetic and electric fields at all points in space for all time. The only limit on resolution and model size is computer memory and processing time. The medium can be completely specified over all space and be made arbitrarily complex by varying any of the material parameters. One technical point, to ensure stability, each direction (i.e. x, y, z) had the medium specified since the field points are not collocated. This allowed for a more accurate representation of curved surfaces since not all three fields were guaranteed to be enclosed by the surface. Using this model, it is possible to look at many different systems.

## *2.2 Model Verification and Limits*

Several tests were performed to ensure the model was accurate. These tests were in general successful, but also revealed some limitations of the model. Understanding the limitations is useful when distinguishing real effects from numerical artifacts during simulations.

The first test performed was measuring reflection and transmission at normal incidence from a boundary. This test was performed using a 1-D simulation. The test simulated a piece of dispersion free glass (with no nonlinearity) in air. Reflections from the front and back faces of the glass (and subsequent re-reflections inside the glass) were the correct intensity as predicted by Fresnel's equations [3]. The second test was of a nonlinear piece of glass surrounded by linear pieces of glass. This tested to see what, if any, type of reflection a discontinuity in nonlinearity would produce. It was found that there was a small reflection (on the order of 0.1%) which had a smaller temporal FWHM than the incoming pulse and the pulse shape was no longer Gaussian. This result agrees with the commonly used model of Kerr nonlinearity:

$$n = n_0 + n_2 I \qquad \boxed{26}$$

Using an estimate for $n_2$ and I, the expected and measured magnitude of the reflection due to index mismatch agree. The decrease in temporal FWHM occurs because for the edges of the pulse, the nonlinear correction is much smaller and hence there is less reflection. For the peak of the pulse, the expected reflection is largest and this causes the pulse to deviate from a Gaussian shape.

The second test performed was to measure the reflection from the absorbing boundary conditions. Ideally, there should be no reflection; however, there is always some. Also, the percent reflection changes depending on the angle of incidence and the width of the absorbing medium. To test absorption, either normal incidence or light scattered from a spherical particle was used. Using four cells as an absorbing boundary, the reflection had a worst case of 1% of the incoming light. Using ten cells, the reflection was less than 0.01% for all angles of incidence. For this reason, all absorbing boundaries were kept at least ten cells wide to reduce numeric error.

The third test was to generate a temporal soliton inside a medium. A soliton occurs when an ultrafast pulse passes through a nonlinear medium and the pulse neither broadens nor steepens and retains its original profile. This occurs when dispersion and self-steepening exactly cancel each other. This type of experiment had been done before using FDTD [6] and we reproduced those results. In the experiment, a femtosecond pulse impinges on fused silica. Using the correct intensity, dispersion parameters and strength of the nonlinearity, soliton behaviour with the rise of a daughter pulse (also seen in [6]) was observed. If dispersion was increased, pulse broadening occurred instead. If dispersion was reduced, a higher intensity was used or a larger Kerr nonlinearity was used than previously, carrier and/or envelope self-steepening was observed. Depending on the parameters chosen, either carrier or envelope shock could be induced. This behaviour had been predicted before using a different approach [12] and our results agree with their predictions.

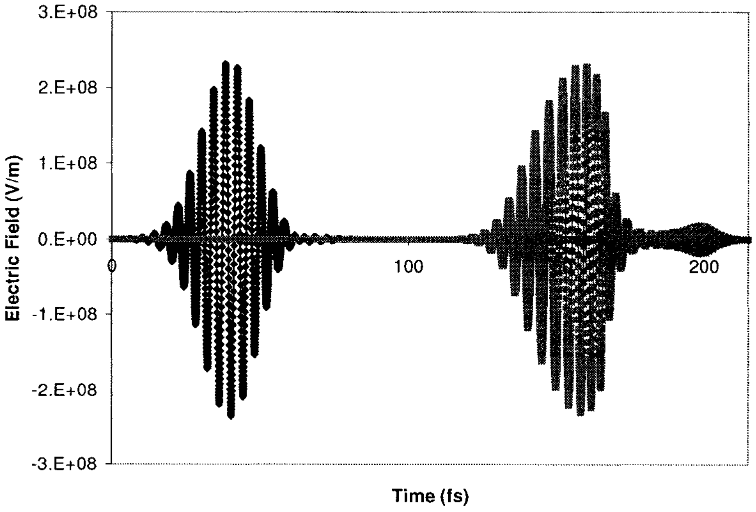

Figure 1. Envelope self-steepening after passing through a medium.

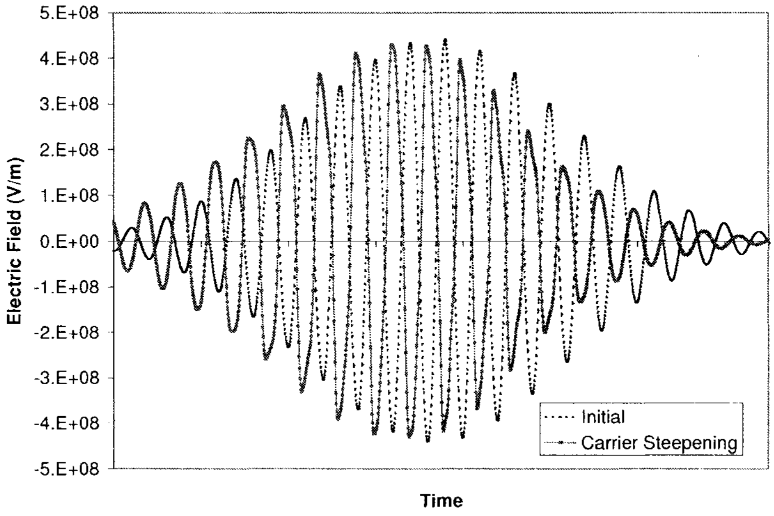

Figure 2. Carrier self-steepening, pulses overlapped for comparison (pulses 100 fs standard deviation).

This self-steepening behaviour represents a limitation on the model. In a physical system, self-steepening would occur until either an optical shock occurred, or dispersion spread the pulse. However, while this self-steepening is occurring, high frequencies are generated in the pulse. Using FDTD, normally one requires that the cell size be smaller than $\lambda/10$ [4]. As the high frequencies are generated, this condition is violated. Once this occurs, the program eventually becomes numerically unstable, and the electric field begins to grow exponentially while generating more high frequency components. This type of instability limits what can be modelled physically. It is a particular problem when combined with 2-D or 3-D simulations since self-focussing increases the peak intensity and hence the amount of self-steepening that occurs. If one point in the simulation reaches a critical instability, the instability will spread or cause the simulation to fail entirely. This type of instability can occur with either Kerr or Raman nonlinearities, but normally the Raman nonlinearity must be resonant and larger than the Kerr nonlinearity needed to generate similar effects.

As mentioned above, self-focussing may be observed in 2-D or 3-D. This only occurs if using a Gaussian pulse or light which has been scattered from an object (self-focussing requires an inhomogeneous spatial profile). This was observed while testing to ensure that diffraction occurs if using a tightly focussed Gaussian beam. To test this, the one edge of the medium is taken to be the focal plane of a Gaussian beam. The beam was then allowed to propagate freely with absorbing boundary conditions on the sides. With this arrangement, diffraction was observed when no medium was present. However, if a nonlinear medium was present, diffraction was reduced. In principle, it is possible to choose medium parameters to generate a spatial soliton (diffraction and self-focussing cancel) which is analogous to the temporal soliton generated previously, but this was not attempted during testing.

One limitation related to focussing was that the paraxial approximation was used to represent the Gaussian beam. Using the paraxial approximation, it is not possible to generate a wavefront which will become a subwavelength beam spot as the beam propagates (the beam will only focus to a wavelength size spot or greater). This led to problems if one wanted to have the focal plane in the center of the medium. This limitation could be overcome by using the proper tightly focussed representation first outlined by Richards and Wolf [13]; however, for our applications, this was not a concern and the increase in complexity was not needed since we used the front face of the medium as the focal plane for a Gaussian beam.

The final test was to ensure that the Raman nonlinearity behaved correctly for the generation of a CARS signal. For this test, we used a resonant Raman term along with nonresonant terms (one electronic and one Raman nonresonant term) and observed changes in the CARS signal generated in the forward direction (for further explanation of the resonant and nonresonant terms, see section 4.1). It can be shown [14] that the CARS signal strength is dependent on the nonlinear susceptibility, pump intensity and the Stokes intensity:

$$S_{CARS}(\omega_{AS}) \propto \left|\chi^{(3)}_{CARS}\right|^2 I_P^2 I_S \qquad \boxed{27}$$

The first test of our Raman model was to measure the dependence of the CARS signal on the pump and Stokes intensity. From equation (27), we expect a linear dependence on the Stokes intensity and a quadratic dependence on the pump intensity. Our model matches these expectations quite well as may be seen in the figures below:

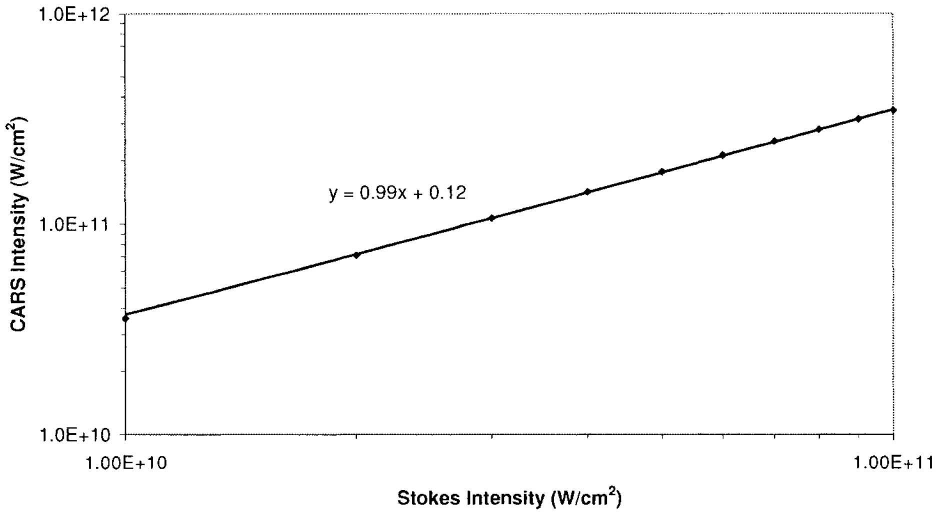

Figure 3. CARS signal dependence on Stokes intensity (log-log plot).

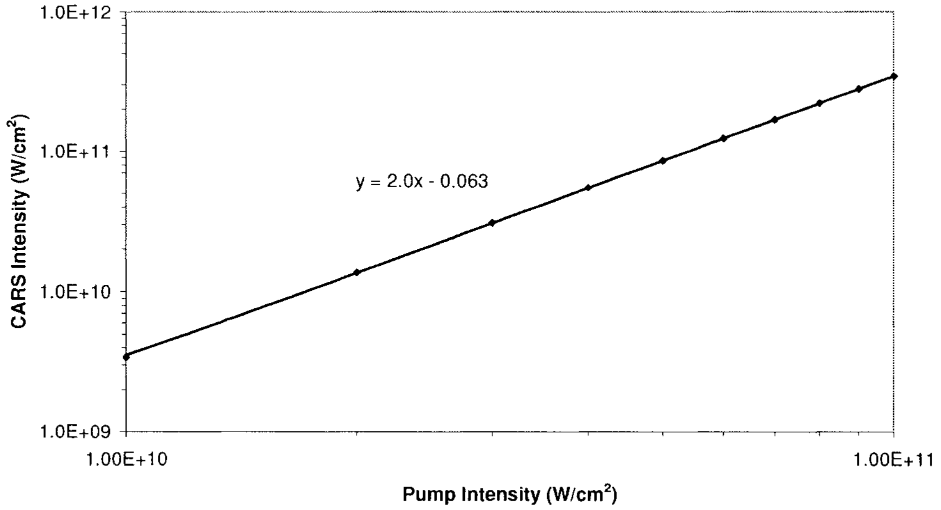

Figure 4. CARS signal dependence on pump intensity (log-log plot).

A second test of CARS generation was to examine the line shape of the CARS signal when the frequency difference between the pump and Stokes was tuned away from resonance. To predict the line shape, we must expand the expression for the susceptibility in (27). Neglecting one photon resonances, the third order susceptibility may be obtained from perturbation theory [15]:

$$\chi^{(3)}_{CARS} = \eta_{NR} + \frac{A_t}{\omega - 2\omega_P - i\Gamma_t} + \frac{A_t}{\omega - (\omega_P + \omega_S) - i\Gamma_t} + \frac{A_t}{\omega - 2\omega_S - i\Gamma_t} + \sum_R \left[ \frac{A_R}{\omega - (\omega_P - \omega_S) - i\Gamma_R} \right] \qquad \boxed{28}$$

where $\eta_{NR}$ represents nonresonant, frequency independent electronic contributions (frequency independent since the terms are far from resonance), t denotes two-photon electronic transitions, R denotes Raman transitions and A is the scaling factor for the strength of the transition. If near-IR frequencies are used, all of the electronic and nonresonant Raman contributions can be combined into one nonresonant term as $\chi_{NR}$ [15]. This allows us to expand equation (27) in terms of resonant and nonresonant contributions:

$$S_{CARS} \propto \left|\chi_R^{(3)}\right|^2 + 2\chi_{NR}^{(3)}\left\{\mathrm{Re}\left(\chi_R^{(3)}\right)\right\} + \left|\chi_{NR}^{(3)}\right|^2 \qquad \boxed{29}$$

From equation (29), we see that there are different contributions to the expected line shape of the CARS signal as the signal is detuned from resonance. There is a frequency independent nonresonant term, a frequency dependent resonant term and a mixing term which is proportional to the real part of the resonant term. The parameters used for the simulations below are the same as those used in section 4.3. The three constituents of $\chi^{(3)}$ are illustrated in figure 5:

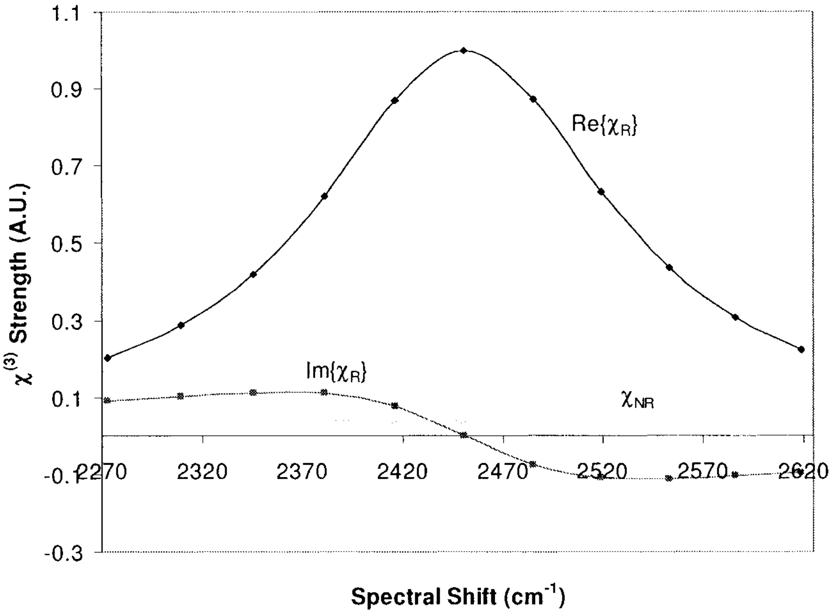

Figure 5. Different contributions to CARS line shape (typical max value is 1e-20 $(m/V)^2$).

We can compare the line shape generated using the FDTD model and our predicted line shape which is the sum of the three constituents. This may be seen in figure 6:

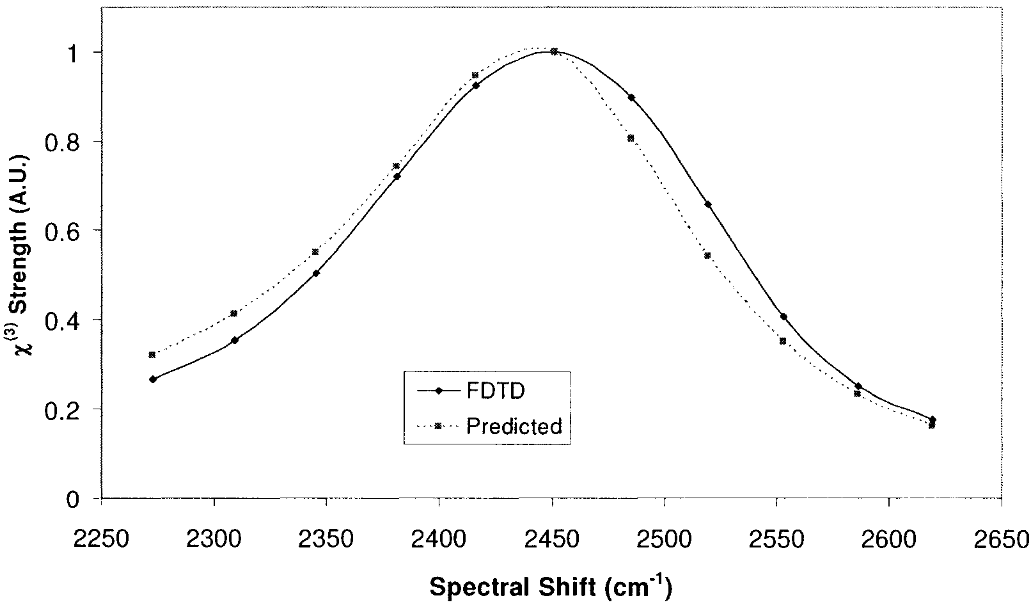

Figure 6. Theoretical and FDTD CARS line shape near resonance (typical max value is 1e-20 $(m/V)^2$).

We see from figure 6 that the FDTD model matches the predicted line shape reasonably well. There is a slight deviation for detuning below resonance and larger deviation above resonance; however, the deviations are not significant while operating on resonance. This confirms our use of the model for CARS signal generation and allows us to proceed with confidence in further experiments.

The testing undertaken illustrated that the model chosen agrees well with physical systems. It also illustrated the one significant limitation of the model. High intensity or strong nonlinearity can cause catastrophic self-steepening. This leads to a numerical instability which generates an unphysical electric field. This can become an issue if any point in the system has a very high intensity. For example some experiments were limited since focussing and/or local field enhancements due to scattering increased the electric field to unsustainable levels. This could be overcome by using techniques where the cell size is variable and regions of instability have smaller cell size [4]. However, these multigridding techniques greatly complicate the code while providing little benefit if there are many regions which may experience instability (since most of the code must switched to a small grid size) or the regions of instability are unknown prior to running the simulation. Both drawbacks of multigridding affected our scattering simulations. For such cases where instability did occur, either the geometry was changed or the pulse intensity was reduced to ensure stability. In general the model gives an accurate representation of physical systems and allows us to proceed with confidence for future experiments.

# 3 Myelin Sheath

A first test case for the model was provided by Dr. Andy Risdale of the Ottawa Health Research Institute (OHRI). Dr. Risdale had taken measurements of live nerve fibers *in vitro* and detected an unusual signal that could not be explained. The signal was a broad bandwidth weak signal that originated from the myelin sheath of the nerve fibers. This signal allowed detailed images of myelinated axons without the addition of exogenous dyes. Dr. Risdale requested we try and determine the origin of this signal in order to determine if it would be viable to use these measurements for further experiments.

## *3.1 Physical Measurements*

The myelin sheath is a highly ordered structure that envelopes the main nerve axon and is found around most nerves. The myelin is white; hence giving rise to the name white matter (it is not present in grey matter). Its main function is to assists in the conduction of action potentials along the nerve. The sheath is lipid rich and exhibits birefringence in both the radial and axial directions [16]. In large nerves, individual fibers are bound together by collagen to form one bundle. In the experiments performed, individual axons were studied by first physically separating the axons at the ends of the main bundle. The axons were then examined after treating the nerve bundle with collagenase which removed the binding collagen and allowed the fibers to separate.

To examine the nerves, a microscope using a femtosecond laser operating around 800 nm was used as the light source. The pulses were approximately 60 fs long and the average power at the sample was varied from 20 to 80 mW. An oil immersion lens (NA 1.3) was used to focus the light onto the sample. A galvanometer was used to raster scan the sample for each image. The raster scanning allowed examination of the whole structure while ensuring heating of the sample and possible photo-damage of the sample was minimized.

Two mutually exclusive techniques were used to examine the output signal. Using dichroic mirrors and short pass filters, the spectrum of the entire signal could be examined by blocking all wavelengths greater than 680 nm (effectively blocking the incoming laser pulse and any scattered light from that pulse). The spectrometer used to measure the signal had a functional measurement range of approximately 400 to 700 nm. Time-correlated single photon counting (TCSPC) was used for time resolved measurements of the signal. The time measurements were calibrated to use the laser pulse as time zero and provided picosecond time resolved measurements of signal decay.

When the bulk nerve fiber was examined, very little signal in either the forward or backward direction was observed. When nerve endings that had been physically separated were examined, a second-harmonic generation (SHG) was observed. This signal closely resembled the signal which may be observed from collagen taken from other parts of the body. Furthermore, the body collagen and the nerve fiber collagen-axon mixture exhibit a similar fibrous structure when imaged, as may be seen in figure 7. The second harmonic signal is much stronger in forward direction for both samples.

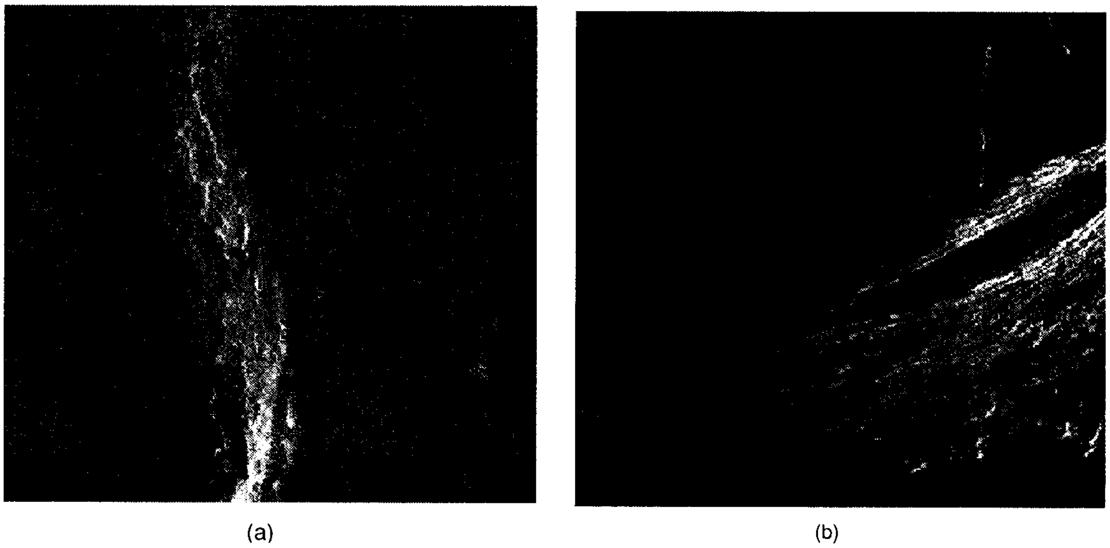

Figure 7. Second harmonic generation from (a) nerves (running up the page) and (b) collagen (across the page).

After the nerve had been treated with collagenase, a weak broadband signal could be observed. Most of the individual fibers exhibited a signal of similar strength which was localized to the myelin. This signal allowed detailed images of the myelin morphology to be taken since the axon only weakly emitted.

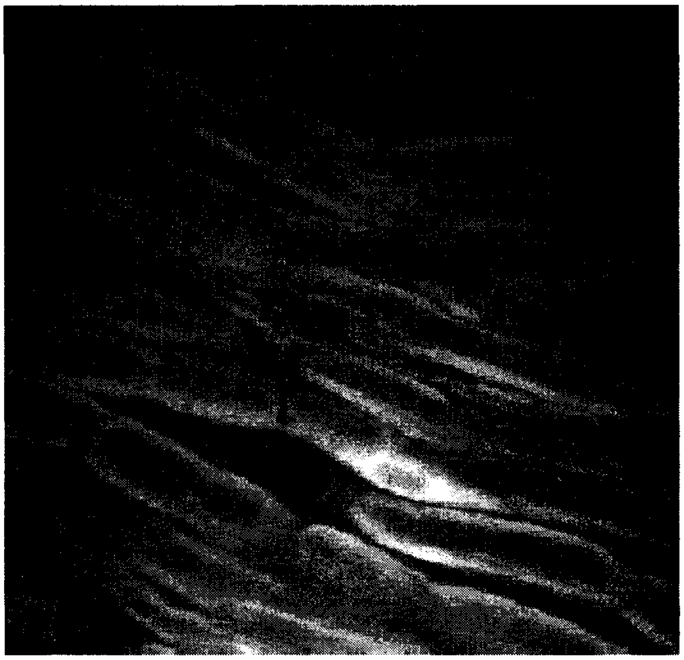

Figure 8. Broadband signal emitted from the myelin sheath.

The signal was detected in both the forward and backward directions and has a similar spectrum in each direction (overall intensity in the forward and backward direction was not assessed by Dr. Risdale). The epi-detected (backward directed) signal was much weaker than the light scattered by the incoming laser pulse (without the short pass filter, the signal could not be distinguished). A sample spectrum taken in the epi-direction is included below.

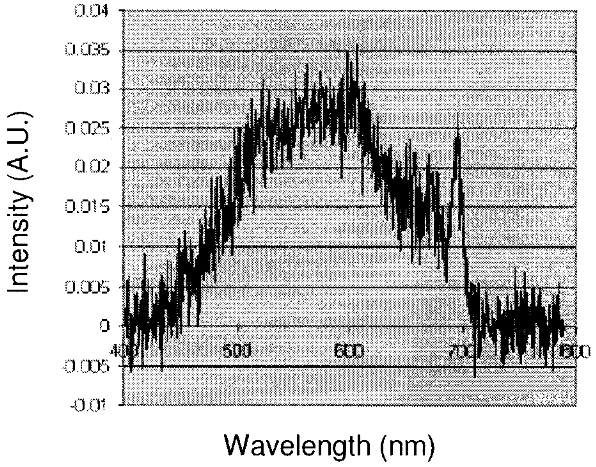

Figure 9. Epi-detected broadband spectrum emitted by myelin sheath (the peak at 690 nm is the tail end of the excitation pulse).

Using time-resolved measurements, it was found the signal contains at least two decay terms (it was not possible to determine if an instantaneous nonlinear signal was present). The two decay terms had decay constants of approximately 0.5 ns and 2.8 ns. This type of decay is characteristic of fluorescence and this is the likely source of such behaviour. Unfortunately, as mentioned above, it was not possible to differentiate which frequencies were emitted at which times.

### *3.2 Simulations*

Our initial hypothesis was that the myelin sheath has a significantly larger third order susceptibility than the axon, leading to a much larger nonlinear signal caused by self-phase modulation. SHG may contribute since the fiber is birefringent, but the broad bandwidth of the emitted signal is consistent with self-phase modulation If this is the case, the likely reason this signal is not seen in the bundled fiber (and in the separated ends) is that the presence of the collagen scatters the incoming light, limiting the generation of the signal. Furthermore, if self-phase modulation is the predominant method of generating the signal, we would expect a strong signal in the forward direction but a very weak signal in the epi-direction since the only backwards going signal should originate from reflections from the various interfaces present. This would be consistent with observed signal. Finally, the fact that the myelin is a dense, ordered structure lends credence to the hypothesis that the nonlinear susceptibility would be higher than that of the axon which is much less dense and is heterogeneous.

To model the axons, a simple model was chosen of two concentric cylinders. Since the axons are very long axially (perpendicular to the direction of laser propagation), a 2-D model was used (periodic in y, absorbing boundaries in x and z). The individual axons vary in size but are on average approximately 10 μm in diameter with the myelin sheath having a width of approximately 1μm which surrounds the axon. The geometry used is illustrated in figure 10.

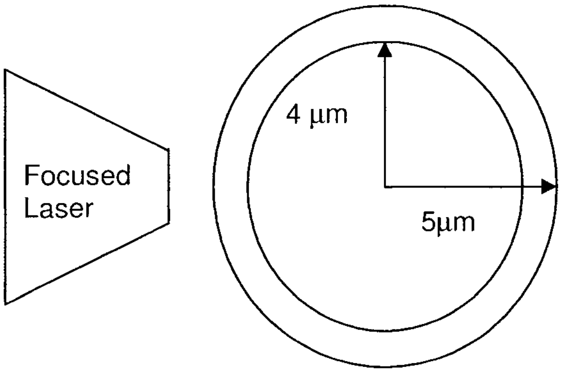

Figure 10. Geometry used to represent myelinated axon.

Two sets of simulations were performed. For the simulations, less intense but shorter femtosecond pulses were used to excite the medium than were used in experiments. This was done since instabilities due to self-steepening were observed in some simulations. The first set of simulations was two 1-D simulations which ignored the curvature of the nerve and the Gaussian spatial profile of the incoming pulse. The first 1-D simulation was of two thin highly nonlinear surfaces surrounding a weakly nonlinear bulk (i.e. pulse hitting the central axis of the nerve). The second 1-D simulation was a shorter bulk substance which was highly nonlinear. This represents hitting the nerve off axis and only interacting with the myelin sheath. For these experiments, the Raman nonlinearity was insignificant, the weakly nonlinear medium had $\chi^{(3)}_{\text{Kerr}}$ = 1e-21 (m/V)$^2$ (similar to water) while the highly nonlinear medium had $\chi^{(3)}_{\text{Kerr}}$ = 1e-18 (m/V)$^2$. The center wavelength used was 790 nm. For both simulations, the epi-detected spectrum was examined. The results of the 1-D simulation support our hypothesis and are included below.

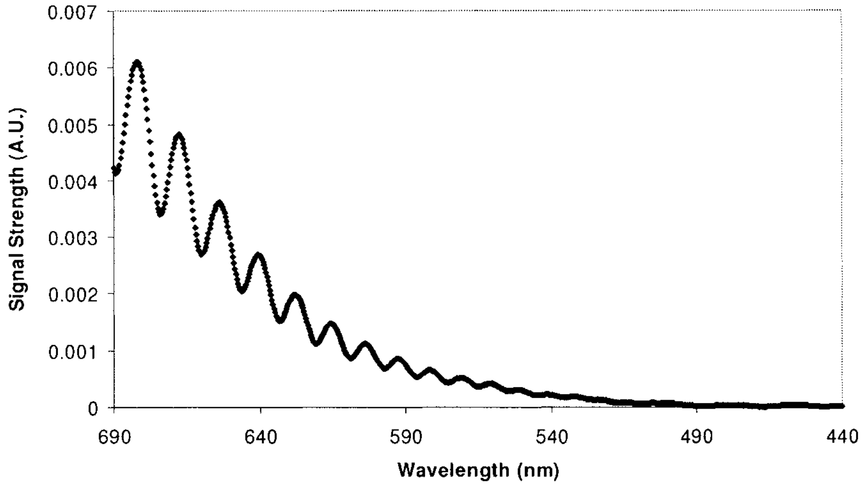

Figure 11. Spectrum from 1-D Simulation: Centered on Axon.

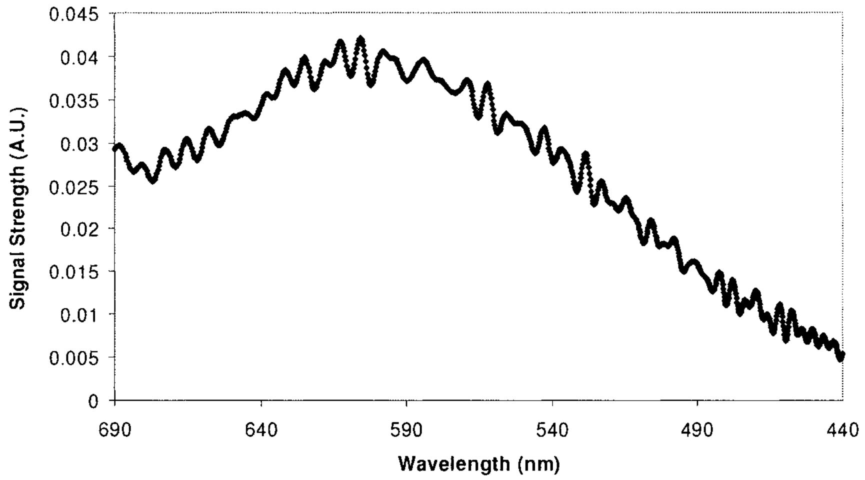

Figure 12. Spectrum from 1-D Simulation: Through Myelin Only.

For the 2-D simulations a tightly focussed Gaussian (objective of NA = 1.2) pulse was used to probe the structure with the incoming pulse being either on or off axis. The off-axis pulse was positioned so that the center of the pulse struck just beyond the axon-myelin sheath boundary. Again, the spectrum of the epi-detected field was then examined for each case.

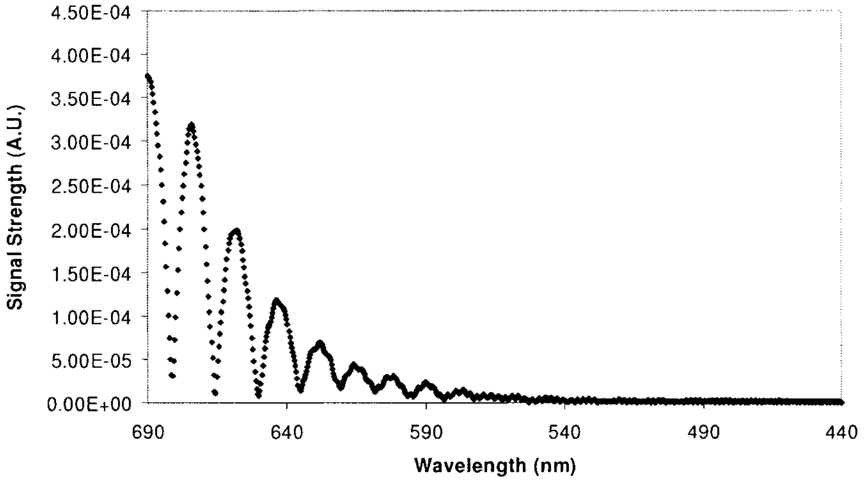

Figure 13. Spectrum from 2-D Simulation: Centered on Axon.

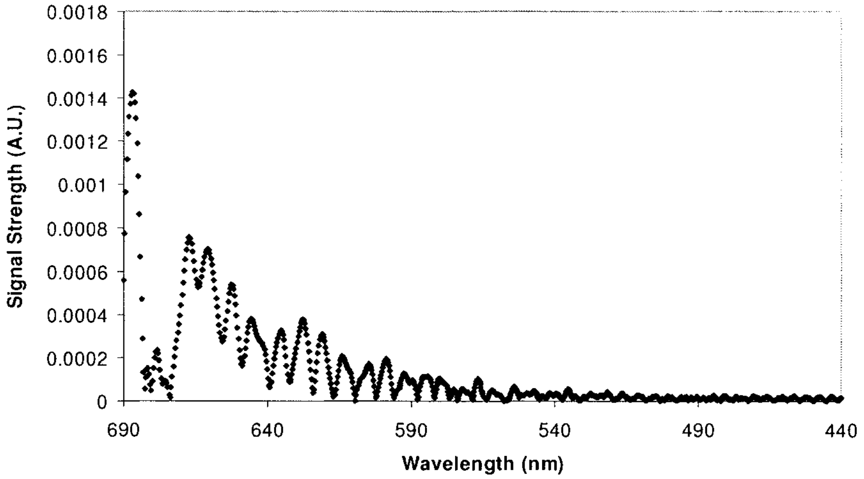

Figure 14. Spectrum from 2-D Simulation: Off-Center of Axon.

From the spectrums in figures 11 and 13, we see that the epi-detected signal from the center of the axon is very small and is mostly due to the tail edge of the incoming pulse. However, the signal from the off-axis has a much stronger nonlinear signal which exhibits the broadband nature that had been previously measured, as may be seen by comparing figures 9 and 12. The 2-D equivalent in figure 14 does not agree quite as well. One likely reason for this is the placing the focal plane of the pulse before the axon. In the experiments, the pulse was focussed inside the nerve (along the midplane). In our simulations, the pulse has already diffracted by the time it reaches the myelin with the diffraction being even larger for the off-axis case. Higher input intensity could correct for this, but that led to instability. Furthermore, if the intensity of the 1-D simulation is reduced, the spectrum of the detected signal closely resembles figure 14. These results would seem to confirm our hypothesis that most of the broadband signal comes from continuum generation in the myelin sheath.

To truly confirm our hypothesis, additional tests are required. We would expect that the spectrum to become less broad as the incoming laser intensity is decreased since spectral broadening is proportional to the intensity (increasing the intensity leads to damage and plasma generation which gives a much different signal). We would also expect the forward propagating signal to be much stronger than the epi-detected signal since the epi-signal likely only comes from reflections.

If our hypothesis of a large nonlinear susceptibility being present in the myelin sheath is confirmed, this opens up a few possibilities. First, this would represent a new way of studying nerves using nonlinear microscopy. Many diseases (e.g. multiple sclerosis) are tied to destruction of the myelin sheath. Using this new form of microscopy may present a new way to monitor and study these diseases. Second, if the susceptibility is very large, this may provide clues on ways to design new highly nonlinear organic polymers. This is an area of active research and having a new physical system to examine will offer insight into possible new design approaches. Finally, it may be possible to utilize the myelin sheath itself for some applications. It is biologically compatible and may prove useful in some designs.

# 4 CARS Microscopy

CARS microscopy is a type of nonlinear microscopy which shows great potential for work with biological systems. The ability to achieve chemical specificity with high resolution and 3-D sectioning achieves the three main objectives of optical microscopy. When CARS microscopy was first demonstrated, there were many problems which limited its use. However, in recent years, new techniques have been developed which have greatly advanced the field and achieved new levels of sensitivity. However, resolution has not improved significantly beyond what was initially achieved. We propose new technique which has the potential to achieve much higher axial resolution than any current nonlinear microscopy (excluding NSOM) which will be called interferometric CARS microscopy or I-CARS. To test this proposed technique, the FDTD model developed was used to test the predicted resolution. These tests agreed with the prediction. A few possible applications of this new technique are presented to conclude.

## *4.1 Introduction to CARS Microscopy*

CARS spectroscopy was first demonstrated by Maker and Tehrune [17] in 1965 and has been used as a tool for chemical spectroscopy of many systems since. Duncan et al. [18, 19] first combined CARS with microscopy using visible dye lasers. However, the required phase matching geometry was difficult to implement with a traditional microscope and required noncollinear input beams. Also, the use of visible light for the pump and Stokes signals led to a large nonresonant background signal due to autofluorescence. This limited its applicability since the nonresonant background is not chemical specific. In 1999, Zumbusch [20] et al. sparked renewed interest in CARS microscopy by employing near-infrared lasers in a collinear geometry. The use of tight focussing ensured phase matching was satisfied in the forward direction [20] making signal detection substantially easier while near-infrared lasers reduced the nonresonant background. The phase matching condition (see figure 15) is relaxed for tight focussing because the short interaction length and the large cone angle of wave vectors near the focus ensures phase matching occurs.

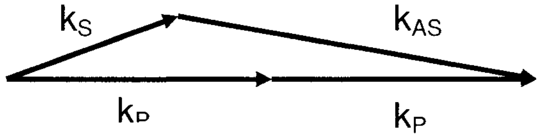

Figure 15. Phase matching condition for CARS generation: $k_s$ is the Stokes wavevector, $k_p$ the pump and $k_{as}$ the anti-Stokes.

While the nonresonant background was reduced, it remained the limiting factor to achieving higher sensitivity using CARS microscopy. To illustrate this, we look at the generation of the CARS signal in a medium:

$$P_{CARS} = \sum P_{NR} + P_R = \left(\sum \chi_{NR} + \chi_R\right) E_P E_{P'} E_S^* \qquad \boxed{30}$$

where NR stands for nonresonant, R for resonant, P for pump, P' for probe and S for Stokes. In most experimental situations, the same frequency is used for the pump and probe. The resonant susceptibility is due the Raman susceptibility of the molecules which will be enhanced if the pump and Stokes pulses are tuned to the vibrational mode of the molecule. The nonresonant signal is generated by either nonresonant Raman modes or nonresonant electronic nonlinearities. These three methods of generation are illustrated below

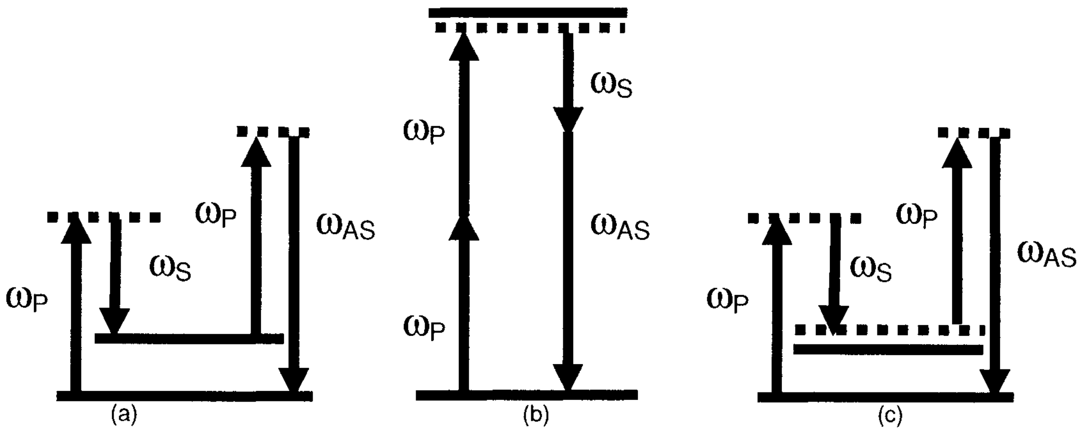

Figure 16. Three methods of generating the anti-Stokes signal, dashed lines are virtual states, solid real states (a) resonant Raman (b) nonresonant electronic (c) nonresonant Raman.

In many cases, the number of resonant vibrational modes is small and hence the resonant signal is weak. If the nonresonant signal is large in this case, this will limit detection sensitivity. Several techniques have been developed to reduce this nonresonant background. The easiest technique to reduce nonresonant background is to use longer pulses since this give enhanced spectral resolution. By having the spectral width of the incoming pulses approximately the same as the Raman line width, most of the energy should go into the desired mode. This requires a laser source(s) which can generate phase-matched, tuneable picosecond pulses in the near-infrared, for example from an optical parametric oscillator (OPO). There are cases where using femtosecond pump pulses is desirable (multiplex-CARS which allows one to study many vibrational modes simultaneously), but for most cases, longer pulses are desirable.

Another common technique for eliminating the nonresonant background signal is to make use of epi-detection (E-CARS) [21]. As mentioned above, tight focussing leads to the phase matching condition for CARS generation to be met in the forward direction. The large cone angle of the focus simultaneously allows for the CARS signal to be generated in the epi-direction. However, because of phase mismatch, there is no signal emitted from the bulk material surrounding the resonant particle. Therefore, in the epi-direction, only subwavelength resonant particles are detected (see section 4.2 for further explanation of E-CARS signal generation).

A third way to reduce the nonresonant background is to use counter-propagating pump and Stokes beams which are overlapped at the focus (C-CARS) [15]. This ensures that the CARS signal is only generated from the desired volume. The nonresonant background is normally generated from outside the focal volume, and this is eliminated using C-CARS. Unfortunately, the temporal and spatial overlap necessary using C-CARS can be difficult to implement, limiting the applicability of this technique for many samples.

Polarization sensitive CARS (P-CARS) microscopy relies on the difference in depolarization ratios for the nonresonant and resonant signal [22]. Using a pump and Stokes which are not polarized in the same direction, the nonresonant and resonant signal will also be polarized in different directions related to the difference in depolarization ratios. By using a polarizer in the output beam path, it is then possible to extract a signal which is due only to the resonant portion (within the limits imposed by the polarizer extinction ratio). Even with a large change in the polarization of the resonant and nonresonant signals, there is always some rejection of the resonant signal. If the change is small, this rejection prevents effective detection of the sample since too much of the resonant signal is rejected.

Coherent control [23, 24] is another method of reducing nonresonant background. With this technique, spectral phase control allows one to interfere the quantum pathways in a molecule so that only resonant signal is generated and nonresonant signal is suppressed. Using this technique, background free CARS using a single femtosecond pulse has been demonstrated [25]. In highly heterogeneous structures, or when using scanning mirrors, this technique can be difficult to implement since it becomes more difficult to overlap all the frequencies at one point in space.

A final technique which has been used for background suppression is pulse-sequenced CARS [26]. If the pump and Stokes pulses are tuned to a resonant vibrational level, some population will remain in that level even after the probe pulse interacts with the sample. However, for nonresonant transitions, there will be no population remaining. Therefore, if a second, time delayed probe pulse is used, a second CARS signal is generated from the remaining excited population. This may be thought of as the resonant level having a much longer dephasing time than the nonresonant levels. The signal from this technique is much weaker than the initial signal since the excited population is much smaller than when the pulses are overlapped.

While all of the above techniques offer improvements in CARS microscopy, they all address background suppression and sensitivity. Other than using NSOM CARS [27, 28], there has been no technique demonstrated to offer improvements in the resolution of CARS microscopy beyond those inherent to nonlinear microscopy. The coherent nature of the CARS signal allows one to design an experiment that would show significant improvements in the axial resolution.

## *4.2 Interferometric CARS*

Under tight focussing, we expect the phase of the incoming pump and Stokes beams to be changing due to the Gouy phase shift and propagation effects. Since the Gouy phase shift is affecting both beams, we will ignore it for the time being and instead focus on propagation effects. First we examine the change in phase of the forward propagating CARS (F-CARS) signal at the detector if a point particle moves inside the focal volume.

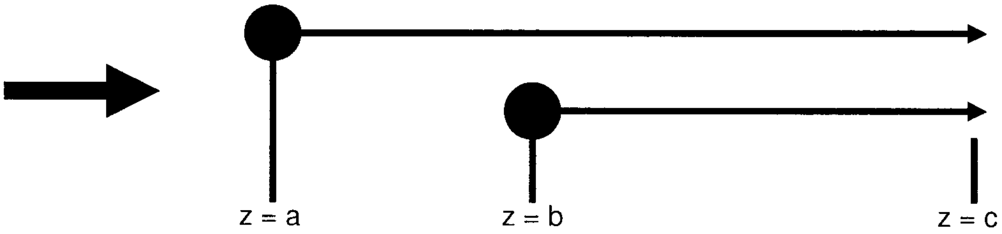

Figure 17. F-CARS signal generated by two point particles located inside a focal volume.

The signal at detected at C due to a particle A is given by:

$$E_{CA} = E_A \exp(ik_{CARS}(c-a)) \qquad \boxed{31}$$

while the signal at C due to B is given by:

$$E_{CB} = E_B \exp(ik_{CARS}(c-b)) \qquad \boxed{32}$$

However, this ignores the change in phase of the pump and Stokes beams as they propagate from A to B (i.e. $E_A$ and $E_B$ do not have the same phase). Taking this into account, we find:

$$E_B = E_A \exp(i(2k_{Pump} - k_{Stokes})(b-a)) \qquad \boxed{33}$$

This can be further simplified by making use of the phase matching condition for CARS:

$$2k_{Pump} - k_{Stokes} = k_{CARS} \qquad \boxed{34}$$

giving us

$$E_{CB} = E_A \exp(ik_{CARS}(c-a)) \qquad \boxed{35}$$

This shows that the CARS signal in the forward direction always adds constructively (hence the large nonresonant signal from a bulk medium). However, this does not hold in the epi-direction.

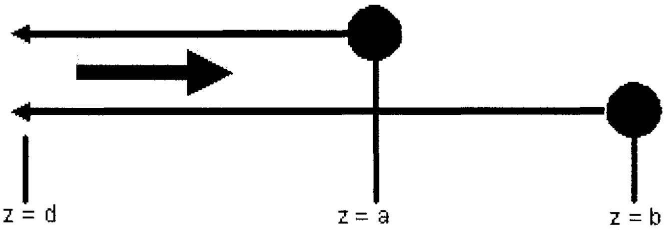

Figure 18. E-CARS signal generated by two point particles located inside a focal volume.

If we again compare the detected CARS signal from two different points, but this time comparing E-CARS signals, we find:

$$E_{DA} = E_A \exp(ik_{CARS}(a-d)) \qquad \boxed{36}$$

$$E_{DB} = E_A \exp(ik_{CARS}(a-d) + 2ik_{CARS}(b-a)) \qquad \boxed{37}$$

We see that the position of the particle in the focal volume changes the phase of the epi-detected signal. When the signal is generated from a bulk medium, all points contribute to the epi-detected signal with a different phase, and hence we have a very small nonresonant signal. However, for a resonant medium which is subwavelength, only a small portion of the Rayleigh range contributes to the signal and this permits some signal to be detected. We expect that the epi-detected signal should initially grow as the particle increases in size since interference will be small but the excitation volume is increasing by a large percentage. Eventually, we should reach a point beyond which the signal will decrease as the size of the sample increases. This increase followed by a decrease as size increase has been confirmed by observation [21] and in models which fully account for tight focussing [15].

The phase change of the epi-detected signal opens up the possibility of a new type of correlation spectroscopy using CARS microscopy. If the epi-detected signal is heterodyned with a reference signal, it is possible extract the phase of the detected signal and from that determine the position of the particle in the focal volume. From (37), we expect the interference signal to have a periodicity of $\lambda_{CARS}/2$, where $\lambda_{CARS}$ is the wavelength of the CARS signal inside the medium. In order to generate the necessary reference signal, either a reflection of the forward going CARS signal can be used, or an externally generated reference.

The first proposed technique would utilize the forward propagating nonresonant signal by reflecting it in the epi-direction. These types of reflections are already present in CARS microscopy, but are insignificant. CARS microscopy is often performed using a confocal microscope. These microscopes use a spatial filer (a pinhole) to reject light emitted from outside the focal volume (this allows 3-D sectioning in linear microscopy). One way to do increase the signal to noise ratio (SNR) of the interference signal would be to relax the usual confocal parameters. By either removing or enlarging the pinhole, more reflected light would be collected at the detector. This would not reduce the axial resolution since the resonant signal is only generated at the focus (and hence provides good axial resolution by default). Ideally, most of the epi-detected nonlinear signal would originate from one strong reflecting surface (e.g. a water-glass interface that naturally occurs in microscopy). This could be artificially designed if the natural back reflections were insufficient (i.e. use a weakly reflecting coating to enhance back reflection).

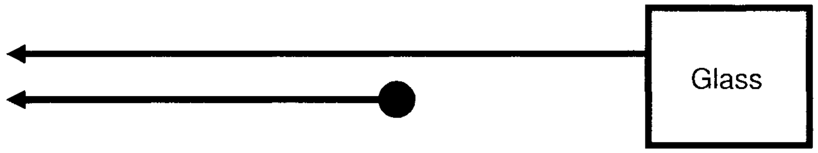

Figure 19. Proposed geometry for reflectance I-CARS.

The use of reflected nonresonant signal has two drawbacks and one advantage over an externally generated reference signal. One significant disadvantage is that there is no outside control of the amplitude of the reference pulse using this technique. Depending on the geometry used, this may appreciably reduce the SNR. The second disadvantage is that this technique requires the resonant medium to move relative to the reflecting one. If a significant part of the reflection is occurring at the interface of the water and the resonant medium, no phase difference will be observed as the particle moves, spoiling the measurement. Also, if the whole sample should move (i.e. the microscope slide moves in the axial direction), this technique will not detect the change since a phase change will not occur. The one important advantage of the reflection pulse technique is that the reference signal is generated locally. This reduces the effect of changing external environment and changes in the medium surrounding the resonant scatterer.

Using an externally generated signal is similar to optical heterodyne detection (OHD), where interference effects may be used to increase sensitivity [29]. For the externally generated signal technique, we would make use of an apparatus similar to a traditional interferometer. A CARS signal would be generated and then overlapped with the incoming pump and Stokes signals. This reference pulse could then be extracted at the microscope and be allowed to interfere with the epi-detected signal. A possible apparatus is outlined below.

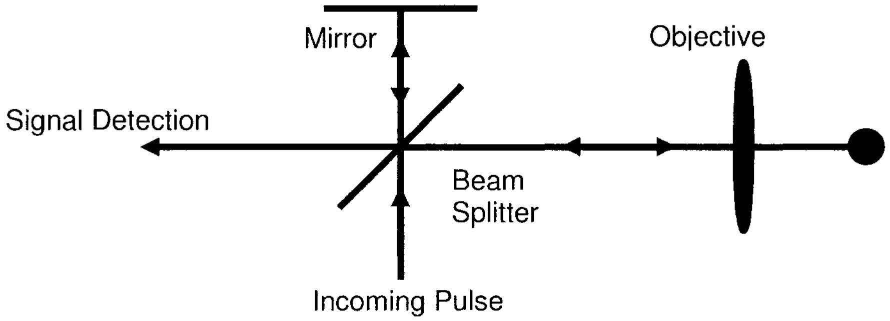

Figure 20. Proposed geometry for OHD I-CARS.

Using an externally generated reference pulse, as one can infer from the above discussion, has two advantages and one disadvantage when compared with the reflected technique. Either during generation or extraction, the external signal can be passed through a variable filter and have the amplitude of the pulse changed to match the epi-detected signal generated by the sample, thereby increasing the SNR. Also, since the extraction mechanism is fixed, movement of the whole sample (i.e. the microscope slide), will still show a change in signal. The one drawback of this technique is the building of an interferometer at the input of the microscope. Using a high NA lens, it would be difficult to place the beamsplitter close to the sample. This forces the interferometer to have long arms with many optics in each arm. This leaves the apparatus prone to vibration and changes of the external environment as well as introducing loss. This is unlikely to be a problem in an optics laboratory, but may be a problem if it is desired to use this technique in a wide range of settings.

It would be possible to combine the two techniques to reduce the drawbacks. By using an externally generated reference pulse which is then reflected, it would be possible to adjust the strength of the reflected pulse. However, this would still have the disadvantage of not being able to detect movement of entire microscope slide. Also, it may prove difficult to phase match the externally generated signal with the locally generated nonresonant signal.

To include the Gouy effect, we will only use the paraxial approximation and not take into account the effects of tight focussing. It has been previously show that for small samples ($<0.75\ \lambda_P$) the ratio E-CARS and F-CARS signals is the same if tight focussing is taken into account or if only the paraxial approximation is used [15]. Furthermore, since the CARS signal is generated at the focus, we will only look at the on axis phase (i.e. ignore change in phase due to the wave-front radius). We also ignore dispersion in finding the phase. This can be justified by the small lengths (less than a wavelength) that the light propagates over while passing through the focus. With these approximations, we find that the Gouy phase shift is given by [15]:

$$\eta(z) = \arctan(z / z_0) \qquad \boxed{38}$$

where $z_0$ is the half the Rayleigh range and is given by

$$z_0 = \frac{k\omega_0^2}{2} \qquad \boxed{39}$$

and $\omega_0$ is given by

$$\omega_0 = \frac{0.61\lambda}{NA\sqrt{2\ln 2}} \qquad \boxed{40}$$

where NA is the numerical aperture of the focussing beam. The phase of the electric field is then given by (for on axis beams only):

$$\phi = kz - \eta(z) \qquad \boxed{41}$$

Taking (41) into account, (36) and (37) must be changed. This then gives:

$$E_{DA} = E_A \exp\{i(k_{CARS}(a-d) - 2\arctan(a/z_P) + \arctan(a/z_s)\} \qquad \boxed{42}$$

$$E_{DB} = E_A \exp\{i(k_{CARS}(a-d) + 2k_{CARS}(b-a) - 2\arctan(b/z_P) + \arctan(b/z_s))\} \qquad \boxed{43}$$

where $z_P$ is the Rayleigh range for the pump and $z_S$ is the Rayleigh range for the Stokes. Comparing equations (36) and (37) with (42) and (43), we see that the Gouy effect will increase the period of the interference signal in the area of the focus. This can be illustrated by plotting the real part of the phase of equations (37) and (43) with "a" taken as zero (particle moving relative to the center of the focus).

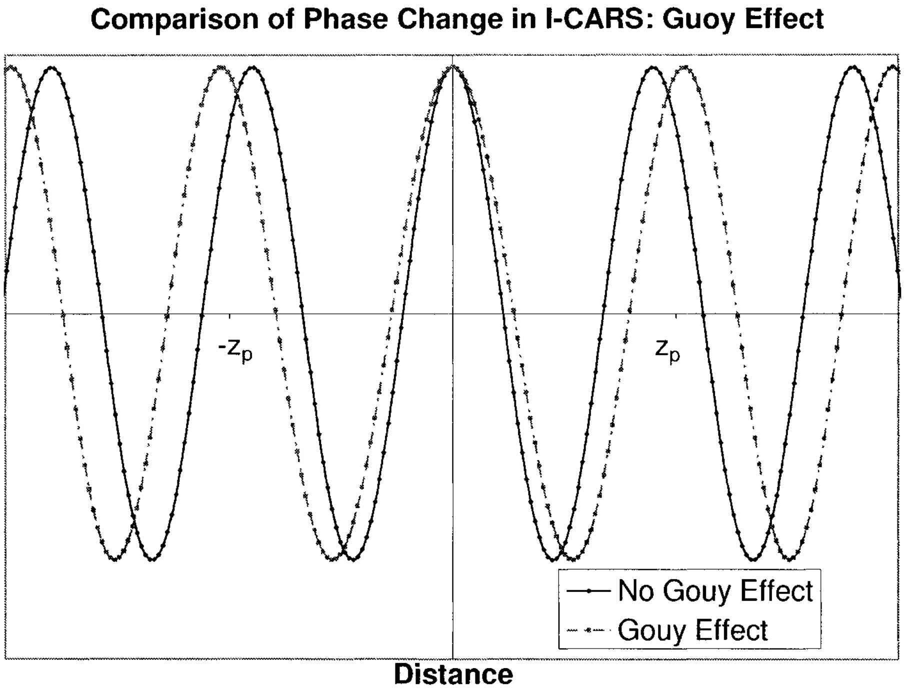

Figure 21. Comparison of phase change at epi-detector: with Gouy effect vs. without.

Notice that in figure 21 there is more than one period inside the pump Rayleigh range (the Stokes has an even larger Rayleigh range). This indicates that even with the decreased periodicity, we still expect the interference signal to be useful in tracking particle movement.

### *4.3 FDTD Test of I-CARS*

To further test this prediction and the viability of the two methods of generating a reference pulse, a 1-D FDTD simulation was performed (periodic boundary conditions in x and y, propagation along z). This simulation ignored the effect of tight focussing (cannot be accounted for in 1-D), but as shown above, this is a minor correction.

To test the reflection pulse technique, three different media were used with a background index of refraction equal to water. The first medium was a nonresonant CARS medium. To specify this medium, the strength of one Raman pole was set to zero while the other was set to be far off resonance. An electronic nonlinearity was also included in the nonresonant medium. A resonant medium was placed inside the nonresonant medium. The resonant had the same nonresonant Raman pole and electronic nonlinearity as the surrounding medium as well as a nonzero resonant Raman pole. For both the nonresonant and resonant media, dispersion was included and matched to water. The final media specified was a glass medium at the end of the nonresonant medium. The glass used a different dispersion relation than the nonresonant and resonant media but did include the same nonresonant nonlinearities as the other two media.

The decision to use the same dispersion relation for the nonresonant and resonant media was made so that the majority of the reflection would be generated by the glass-water interface. The glass medium would not be nearly so close to the resonant sample in practice (only separated by a few hundred nanometers in the simulation), but because focussing and diffraction are being ignored, this does not have a major effect. Also, the glass should be much thicker (millimetres instead of nanometers), but this was necessary to complete the simulation in a realistic time. This thin glass medium will generate a double reflection instead of the desired single reflection, but the narrowness of the medium means that interference between these two reflections is minimized. In a realistic sample, only the first reflection should play a role since we can use the confocal parameters to reject other reflections.

For the externally generated reference pulse, the same sample as above was used except the glass medium was removed. A test simulation allowed us to determine the approximate magnitude required for the external signal. The same external signal was then used for all subsequent runs by adding it to the emitted field.

For both simulations, the resonant medium was moved in the z direction for each new trial. The resonant medium used was 200 nm wide. The pump pulse was 1200 nm while the Stokes pulse was 1700 nm. This gave a CARS wavelength of 927 nm. These wavelengths were chosen arbitrarily and for ease of computation. The pulses used had a FWHM of 140 fs, much shorter than the picosecond pulses normally used for CARS. This was done to speed up computation. To compensate for the broad spectrum the femtosecond pulses have relative to picosecond ones, the Raman resonance used was made wider. Furthermore, the off resonance terms were spaced further from the resonance term than in a real system. All of these changes do not alter the basic physics and do not invalidate the proof of principle experiment while greatly reducing the computational time required. Note, that because focussing was not used, the E-CARS signal is generated for any location of the resonant medium within the limits of dispersion. Because of this, the simulation results extend over a range larger than the Rayleigh range of the pump.

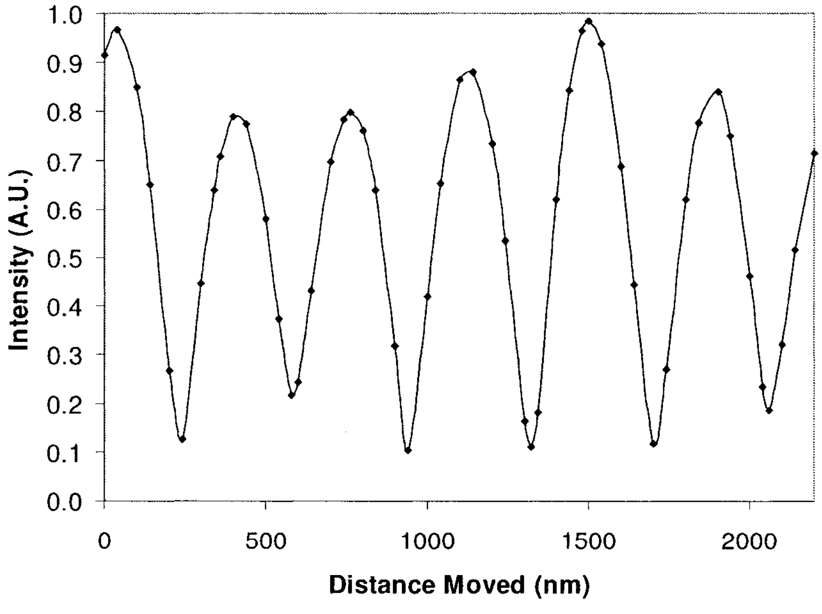

Figure 22. Detected interference signal generated using reflection I-CARS.

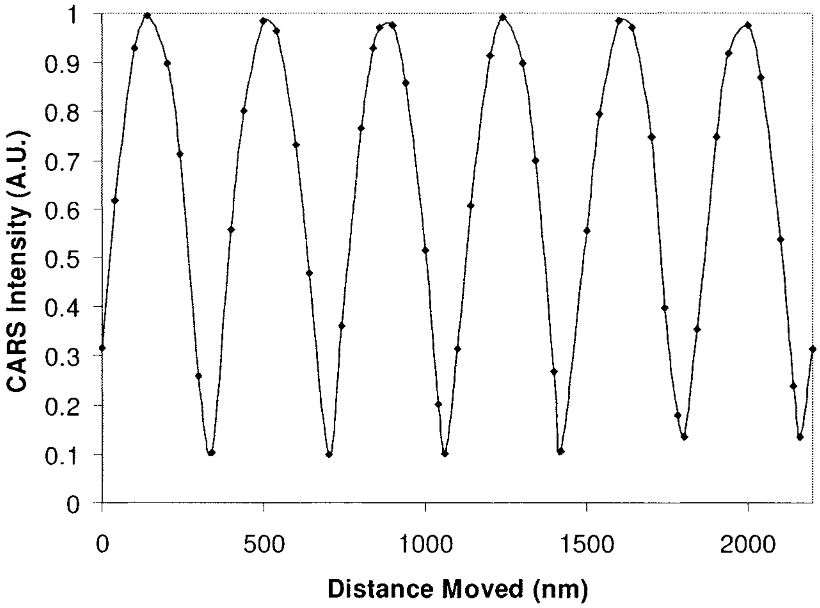

Figure 23. Detected interference signal generated using OHD I-CARS.

Looking at figures 22 and 23, we see that the periodicity is indeed $\lambda_{CARS}/(2n)$. We also see that the external reference pulse technique gives a more uniform interference pattern. This is due to the fact that there is a modulation of the F-CARS resonant signal depending on where the resonant medium is placed. This modulation occurs because the position of the resonant medium changes at which point on the incoming pulses the necessary phase matching occurs. The modulation would be washed out by a much larger nonresonant signal in a real sample.

From figures 22 and 23, we can see that the improvement in axial resolution should be greater than $\lambda_{CARS}/(2n)$. For example, if we measure two points per period (i.e. peak and trough), we achieve a resolution of $\lambda_{CARS}/(4n)$. Depending on the SNR, it should be possible to achieve even higher resolution. Using $\lambda_{CARS}/20$ (between seven and eight points per period or nine or ten points with the Gouy effect taken into account), we can estimate the improvement in resolution that can be achieved in a real system. Using a microscope tuned to improve resolution, an axial resolution of 750 nm using CARS with a pump wavelength of 711.5 nm and a Stokes wavelength 908.3 nm of has been reported while looking at a melamine beads ($\omega_v$ = 3.28 μm) [30]. Using $\lambda_{CARS}/20$, we would expect to get a resolution of approximately 30 nm. If this can be experimentally verified, it would represent an improvement of 25 times over what has been reported.

### *4.4 Applications of I-CARS*

Achieving a resolution of 30 – 50 nm is better than previously reported values for NSOM CARS (128 nm resolution was reported in [27]), but less than some other types of NSOM [27]. However, CARS microscopy can be used to probe objects deep to the surface whereas NSOM is restricted to surface microscopy. More importantly, CARS microscopy does not require the presence of a tip near the sample and can be performed easily on dynamic, live systems. It should be noted that NSOM does posses significantly better lateral resolution, but for some applications, this would not be an issue.

One such application could be the study of the movement of biomembranes inside a dynamic system. A single membrane is approximately 8 nm thick [31], so this technique can monitor membrane movement on a length scale comparable to that of the sample itself. Many different chemical and biological reactions can cause the membrane around a cell to shrink or swell. Using CARS microscopy, it would be possible to monitor this swell on small length scales with microsecond time resolution (assuming kHz repetition rate laser used for image acquisition). For example, when bacteria invade a cell, the two membranes merge and the cellular volumes are combined. This process would be expected to cause the membrane of both cells to shift significantly, and I-CARS should be able to monitor these movement.

Another possible application is studying the effect of protein insertion inside a membrane. Traditionally, to perform this experiment, a membrane is stretched across a glass slide. Proteins are then added to the membrane. Since the proteins are soluble in the membrane, they will settle inside the membrane and change the surround topography and this may be examined using NSOM or AFM, both of which are slow techniques. Using CARS, the system could be quickly scanned in order to measure the change in topography. Furthermore, if more than one protein type is used, once the change in topography was measured, the CARS signal could be tuned to a Raman mode unique to one of the proteins and locate where each type of protein had settled. This could all be performed remotely and in real-time.

A final application that may be possible is monitoring the transport of material in and out of a cell. For some types of material, protein channels are used as guides for transport in and out of the cell. By monitoring these channels, it would be possible to measure the rate of travel inside the channel and estimate the total number of objects being transported in or out of the cell (there are often many channels in one cell). By measuring these factors, it would be possible to measure the dynamic response of a cell to local stimuli rather than rely on average response of many cells. This would be the biological equivalent of monitoring different constituents during a chemical reaction. With current sensitivity limits, this may not be possible; however, sensitivity of CARS microscopy has improved significantly and is likely to continue to do so. When the sensitivity reaches a sufficient threshold, this monitoring of cell flux will likely prove of great interest.

### *4.5 I-CARS: Beyond E-CARS*

The interferometric technique presented using E-CARS can also be used in C-CARS to improve the resolution in both the forward and epi-directions. In the forward direction (forward defined as direction of propagation of the pump beam), the periodicity is half the Stokes wavelength:

$$E_{CA} = E_A \exp(ik_{CARS}(c-a)) \qquad \boxed{44}$$

$$E_{CB} = E_A \exp(ik_{CARS}(c-a) + i2k_s(b-a)) \qquad \boxed{45}$$

In the epi-direction, the period is one quarter of the pump wavelength (which is smaller than half the CARS wavelength):

$$E_{DA} = E_A \exp(ik_{CARS}(a-d)) \qquad \boxed{46}$$

$$E_{DB} = E_A \exp(ik_{CARS}(a-d) + i4k_P) \qquad \boxed{47}$$

However, taking the Gouy effect into account shows that it has more of an effect for the C-CARS case. This occurs because the partial cancellation that occurs for the E-CARS case (the Stokes field is a complex conjugate, hence the Stokes Gouy phase shift subtracts from that of the pump and probe) is instead an addition in this case because of the change in the propagation direction:

$$E_{DA} = E_A \exp\{i(k_{CARS}(a-d) - 2\arctan(a/z_P) - \arctan(a/z_s))\} \qquad \boxed{48}$$

$$E_{DB} = E_A \exp\left\{ i \begin{pmatrix} k_{CARS}(a-d) + 2k_{CARS}(b-a) + 2k_S(b-a) \\ -2\arctan(b/z_P) - \arctan(b/z_s) \end{pmatrix} \right\} \qquad \boxed{49}$$

Using similar reasoning as above and again assuming several sample points per period, we expect a resolution of $\lambda_P/40$. Using the same numbers as above, we would expect a resolution of approximately 18 nm. This is 1.7 times better than when using E-CARS and 42 times better than what has previously been reported. The one problem with using C-CARS is that generating and introducing the reference signal would be more problematic. Also, for non-interferometric CARS, temporal and spatial overlap of the counter-propagating pulses has less strict requirements than would be necessary for I-CARS (adding another layer of difficulty in implementing this technique).

Finally, the interferometric technique introduced here is applicable to any coherent nonlinear signal which is emitted in the epi-direction from a subwavelength source (either a particle or surface). The period of the interference signal will always be $\lambda_{\text{nonlinear}}/2n$. Unless a noncollinear geometry is used, forward going signals will not change phase according to where in the focal volume the particle is located. This technique could be used with SHG, for example, to monitor surface movement (similar to using CARS to monitor membrane movement).

# 5 Microscopic Scatterers

When dealing with nonlinear optics, we are often dealing with mesoscopic heterogeneous systems. The nonlinearity of the system may be contained in the host medium, some dispersed scatterers or both. The scatterers may be dielectrics or metals. These types of systems have been theoretically examined in both the linear and nonlinear regimes, but only with simplifying assumptions which limit the applicability of the solution to certain regimes. The FDTD model that was developed for examining nonlinear microscopy is ideally suited to look at the regimes which are not soluble using analytic arguments.

## *5.1 Introduction to Mesoscopic Scatterers*

A mesoscopic system is generally defined as one where one is not dealing with individual atoms or molecules and it is possible to average over many atoms in order to determine material behaviour, but the system is not macroscopic. For our purposes, mesoscopic refers to a system where the individual components are less than a wavelength of light in length. Some authors require that each component be shorter than a wavelength of light inside the component (i.e. length < $\lambda/n$), but this requirement is not necessary using FDTD.

The linear behaviour of mesoscopic systems has been previously addressed for certain cases. The best known results are those of Lorentz [11], Bruggeman [32], and Maxwell Garnett [33]. Porous silicon has many interesting optical properties in isolation [34, 35] and has been suggested as a possible nanocomposite by filling the pores with another nonlinear substance [36]. Layered structures have been explored both theoretically [37] and experimentally [36, 38].

Lorentz addressed the issue of the local field experienced by a molecule in a homogeneous medium. This correction leads us to expect an enhancement of the nonlinear susceptibility over what is predicted by strictly atomistic theories and is often represented by the Lorentz-Lorenz law. This correction has been covered in many other sources [11, 39] and will not be addressed further.

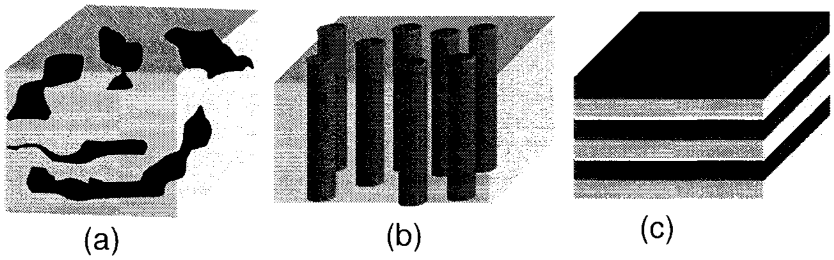

Figure 24. Different mesoscopic geometries: (a) Bruggeman, (b) porous silicon and (c) layered geometry.

The work of Bruggeman dealt with two intermixed components. This may be best thought of as two immiscible liquids which form a chaotic structure. This type of model has been extended to include nonlinearity [40]. Porous silicon may be formed by etching cylindrical holes in silicon. These holes may then be filled with liquids which exhibit nonlinearity. Layered structures are formed using standard deposition techniques and have alternating subwavelength layers which exhibit nonlinearity. These three structures were not investigated during this work, but in principle could be using the FDTD system developed.

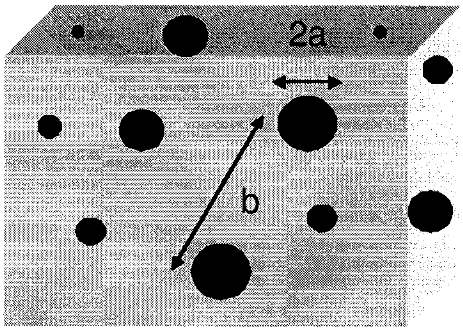

Figure 25. Maxwell Garnett geometry.

We chose to examine Maxwell Garnett structures. These systems are characterized by small spherical inclusions inside a host medium. The decision to look at these systems was made because some kinds of microscopy may be viewed as many independent scatterers which are densely packed. For example, in CARS microscopy, we may investigate a system in which there are many targeted molecules confined to a small volume, but the individual Raman molecules are non-interacting.

Traditionally in Maxwell Garnett systems, it is assumed that the inclusions have radius a and the centers are separated by at least a distance b. Furthermore, it is assumed that $a \ll b \ll \lambda$. These assumptions allow for the prediction of the linear dielectric properties of the system [41 and references therein] and nonlinear susceptibilities [5, 41, 42]. In [5], it is predicted that there will be a reduction of the nonlinear susceptibility if only the inclusions are nonlinear. If the host medium is also nonlinear, however, an enhancement is expected if the dielectric constant of the inclusions is higher than that of the medium. The analysis in [5] extends their results to includes densely packed systems, but the validity of those claims are suspect since the assumption $b \ll \lambda$ can no longer be preserved.

Some of the previous predictions have been corroborated by experiments. A change in the nonlinear susceptibility was measured in [43] using gold nanoparticles in a very dilute solution where the assumption $b \ll \lambda$ still holds (fill factor of $2.2\text{x}10^{-6}$). The experimental results agree well with the predictions made using the same analysis as in [5]. Our simulations dealt with dielectric scatterers, not metallic ones, so it is hard to test these results using our model since part of the enhancement was due to a plasmon resonance.

It should be clarified what is meant by densely packed. In both [5] and [41] the solutions derived make use of a filling factor parameter which may range from zero to one. However, for a face-centered cubic structure, which is the most dense structure that may be created using spheres of the same size, the filling factor is only 0.74. This indicates using a filling factor of one requires changing the geometry under consideration. Furthermore, for randomly dispersed inclusions, the filling factor should be substantially less than 0.74. For our purposes, densely packed includes any arrangement where the inclusions are separated by up to a maximum of five times their radius.

For densely packed systems, individual scatterers cannot be treated in isolation. In this case, adjacent inclusions will have dipole fields which will couple to each other, thereby changing the predicted susceptibility. This coupling of inclusions is not addressed in the previous theoretical work and makes it impossible to predict the change in the composite nonlinear susceptibility for dense packing. Furthermore, scattering from subwavelength structures leads to the generation of a large k-space spectrum (i.e. modes which would normally be evanescent in the dielectric are supported as surface plasmons). Normally these fields cannot propagate since the spectral content of the incoming pulse is exhausted. However, adjacent particles may capture these evanescent fields due to scattering. These fields are not taken into account in the previous theory where only the scattered propagating fields are included.

Other assumptions required by the previous theory may also be tested. The second assumption that a << λ may be tested. In this case, the densely packed case is the only one of interest (otherwise it may be reduced to studying Mie scattering). Another assumption which is used is plane-wave excitation of a medium of infinite extent. This is a good approximation when the incoming light has not been focussed and the medium has a very low fill factor. However, if focussing is used or the fill factor increases, it is not clear that the predicted enhancement should still occur since we expect the scatterers to increase diffraction of the pulse. Finally, the predicted enhancement in susceptibility normally only considers instantaneous Kerr nonlinearity. For Raman nonlinearity, the enhancement may be less since the random scatterers may cause the incoming pulses to no longer be phase matched even though other enhancements may play a role.

## *5.2 Simulations*

As mentioned above, the model being tested was dielectric spherical inclusions inside a second dielectric medium. However, many of the proof of principle ideas were tested in two dimensions rather than three dimensions. A roughly equivalent model of randomly dispersed spheres for two dimensions is randomly dispersed cylinders which are infinite in extent perpendicular to the plane of propagation. In this case, the radius of the cylinder is given by a and the spacing is given by b, the obvious analogs to the three dimensional case. While this model is perhaps better suited to porous silicon, it allows for a simple starting point which requires much less computation than a three dimensional model.

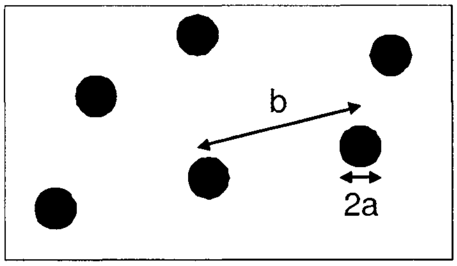

Figure 26. 2-D Geometry used to represent a Maxwell Garnett composite.

The first task was to look for a local field enhancement during scattering. This was done using the two dimensional model with plane wave excitation and absorbing boundary conditions. To test this, we used nonlinear scatterers in vacuum which were densely packed (~ 30% filled). While running these simulations, the program became numerically unstable. The instability was similar to that generated that occurs due to carrier self-steepening. To confirm this and isolate the cause, the electric field over the entire plane of propagation was output previous to the instability occurring. It was observed that the inclusions did not respond instantaneously to the external field and the internal field was in fact weaker than the external one. This is consistent with the fact that the inclusions are dielectric while the host medium is vacuum. It was also observed that the external electric field was amplified when passing between two inclusions. This enhancement effect increased as the inclusions moved closer together. This demonstrates that there is a local field enhancement when inclusions are present. It further demonstrates that tight packing increases the local field enhancement since the field is confined to a smaller spatial volume. This may be illustrated by looking at the figures below.

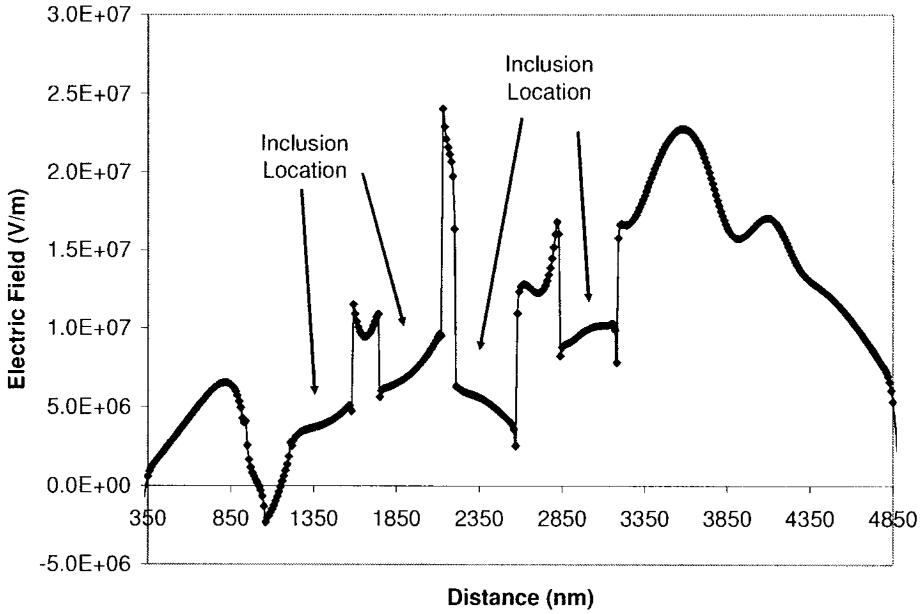

Figure 27. Electric field along transverse cut through medium while propagation is occurring (inclusion radius of 20 nm, spacing of 20 nm).

From figure 27 we see that a large electric field develops between the inclusions. This field leads to large gradients in the electric field (the source of the instability). We would expect enhanced nonlinear effects if the surrounding medium was nonlinear instead of vacuum based on these observations.

The origin of these large fields is due two effects. The first is the multiple scattering of the incoming field. This scattering leads to an enhanced local electric field at some locations while a reduced local electric field at others. This effect is what has been considered in previous work. With this idea in mind, intuitively we would expect this effect to be enhanced as the difference between the dielectric constant of the inclusion and medium increases. This enhancement with increasing dielectric constant has been previously predicted [5]. This enhancement should affect both the inclusions and the host medium since it is a medium range effect. However, since host medium makes up the bulk of the composite, we expect a larger enhancement if the host is nonlinear. Again, this was also predicted in [5].

The second effect which contributes to the field enhancement is due to the subwavelength changes of the dielectric. These changes create sharp edges which are known to generate large local fields for metals [44] and demonstrate similar effects for polarizable dielectrics. There is also a dipole-dipole coupling of nearby inclusions [45] which contributes to the local fields. This effect has not been accounted for in the previous work. It is enhanced as the packing becomes larger and the spacing between particles becomes smaller. Also, as can be seen above, the enhancement is localized to the host medium and has little effect on the inclusions.

For metallic scatterers, the situation is quite different, however. Metal particles can support the large k-vector spectrum generated by the subwavelength scatterers through surface plasmons and the local field can couple to the particles. This then prevents this energy from escaping the system and traps it if the particles are packed densely enough. This leads to a large enhancement. This type of enhancement may be made even larger by using fractal clusters. In this case, small clusters of densely packed particles are dispersed in a medium. The total system has a low filling factor, but the inside of the clusters is very dense. This system will generate local field enhancements from multiple scatterings from the clusters while gaining the benefits of surface plasmon trapping inside the dense clusters. These fractal systems have been demonstrated to have large enhancements over many other systems [45 - 47]. As mentioned earlier, we did not consider metal particles, but qualitatively, we see effects which would agree with the predictions for fractal clusters.

From these 2-D simulations, other effects beyond local field enhancement became apparent. The pulse is delayed passing through the scatterers as opposed to a homogeneous medium. This implies that the pulse experiences temporal compression while inside the scattering medium. We would expect this to increase the local intensity (either inside or outside the inclusions) and thereby lead to enhanced nonlinear effects.

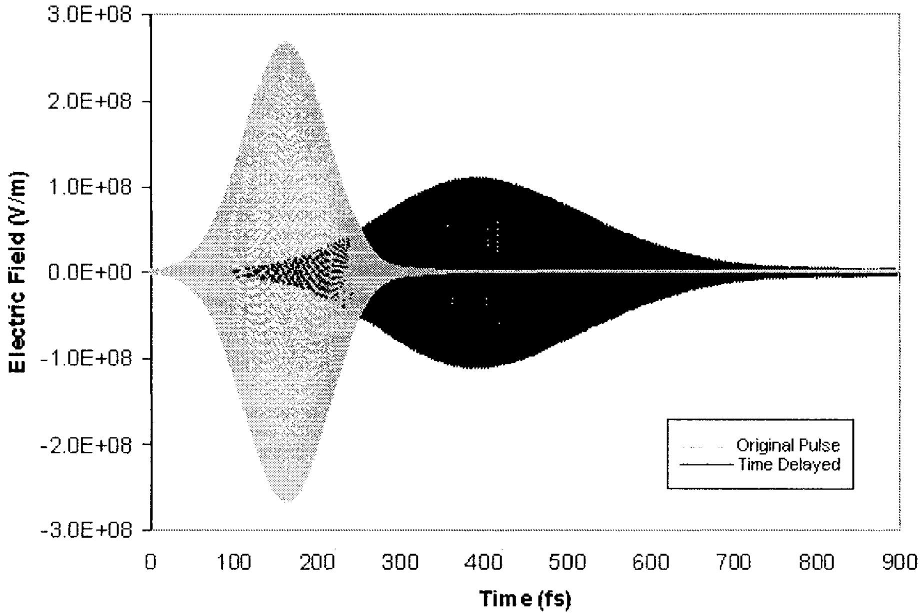

Figure 28. Time delay of pulse through scattered medium (intensity altered for clarity, field from scattered medium generated using periodic boundaries and a dense medium).

A weak optical trapping effect was also observed which became stronger as the density of scatterers increased (the speed of the pulse reduced to as low as c/2). The output pulse was also lengthened considerably in time after passing through the composite. This can clearly be seen in figure 28. This is due to the photons inside the scattering medium experiencing a random walk due to multiple scatterings. The periodic boundaries ensure all energy eventually exits the composite, but this takes time. After the initial compression causing the time delay, the trapped light remains in the nonlinear medium for a much longer time than in the homogeneous case. However, the light is also at much lower intensities. It may contribute to nonlinear signal, but probably plays a small role.

Another effect observed was that the electric field after the scattering medium was very stochastic. Some points had a stronger electric field than in the uniform case whereas other points were much weaker. This of course may be attributed to the interference of the electric field due to multiple scatterings and the random nature of the scattering.

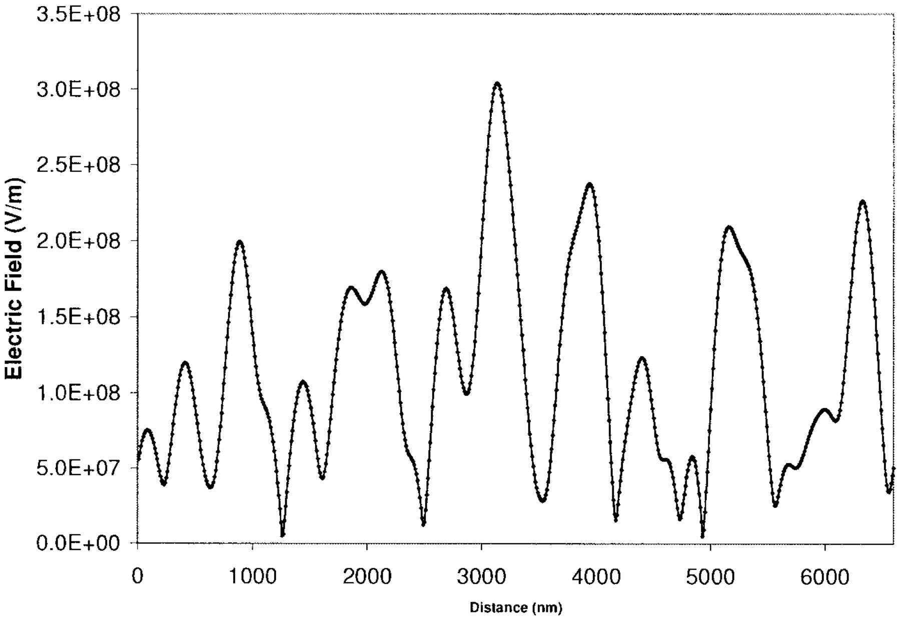

Figure 29. Transverse cut at end of 2-D medium illustrates stochastic nature of signal (periodic boundary conditions with dense medium, input wavelength of 1200 nm).

One other effect of the scatterers was noticed. Depending on the size of the scatterers, the composite acted as a crude frequency selective filter due to unequal scattering and diffraction of different wavelengths of light. To determine if this effect was purely geometrical in nature or related to the nonlinearity of either the scatterers or the medium, simulations were run with only linear scatterers in vacuum using two different frequencies. The short wavelength light was always more strongly scattered than the long wavelength light. Depending where at the output plane the frequency spectrum was measured, the relative strength of the two different frequencies changed greatly. The change in the scattering of the two different frequencies decreased as the scatterers became smaller indicating this is a strictly linear frequency selective behaviour (i.e. particle size determines which frequencies are scattered, the nonlinearity of the system does not play a role).

With confirmation of local field enhancement, it was possible to investigate the effects of this enhancement on nonlinear signals. There were several configurations tested and these will be explained briefly. In the direction of propagation, absorbing boundary conditions were always used. In the two perpendicular directions, either absorbing boundary conditions or periodic boundary conditions were used. The periodic boundary conditions can be thought of as the examination of a small portion of a macroscopic system or a fiber (a real fiber should have reflecting boundaries, not periodic, but for our purposes this is a minor correction). The periodic boundary conditions also replicate the approximations used in the previous work [5, 41]. The inclusions were specified by a radius and a spacing value. The spacing was the minimum distance between the surfaces of two inclusions (not the distance between the centers). The spacing was always kept above zero to ensure the inclusions did not overlap (overlapped inclusions would be more appropriate for random aggregates, but were not studied).

The incoming excitation was always an ultrafast pulse ($\leq$ 100 fs), but it had either a Gaussian or a plane wave spatial profile perpendicular to the direction of propagation. The Gaussian pulse was always taken to have its focal plane at the front of the composite material. Also, the Gaussian pulse was taken to be tightly focussed (spatial FWHM less than a wavelength).

In order to measure the effective nonlinearity, we measured the nonlinear signal generated in the forward direction. This method closely approximates what would be observed during experiments. This also takes into account any reductions in signal due to diffraction or other effects. To measure Kerr and Raman nonlinearities, one or two input pulses respectively were used. If two were used, they were overlapped in time. For Raman nonlinearities, the generated CARS signal was measured. For Kerr nonlinearity, the Fourier spectrum at a point was measured (looking for spectral broadening) and the third harmonic of the incoming pulse was also observed (carrier self-steepening generates a large third harmonic signal). Occasionally, two input pulses were used with a Kerr nonlinearity and the mixing signal (at the CARS frequency) was used as the observable.

The first major conclusion was that using only nonlinear scatterers, there is only a reduction in nonlinear susceptibility compared a uniform medium. This hold for both Kerr and Raman nonlinearities regardless of source or boundary conditions used. This agrees with [5] which predicts that the susceptibility will smoothly increase with fill factor until reaching a maximum when the medium is entirely nonlinear. When considering a medium of infinite extent (i.e. periodic boundary conditions) excited with a Gaussian pulse, this behaviour was observed, but with one major deviation. The susceptibility was found to experience an initial decrease once the medium was broken up into scatterers that was larger than predicted by theory. After this initial unexpected decrease, the susceptibility scaled with fill factor. The initial drop appeared to scale with particle size and became less of a factor as the individual particles became smaller. If absorbing boundary conditions were used, the effective susceptibility (as measured by the amount of signal detected in the forward direction) had a much larger initial decline and did not scale linearly with fill factor.

Looking at Raman nonlinearity in a nonlinear medium with linear scatterers, several interesting observations were made. Using periodic boundary conditions always generated a larger nonlinear signal than an identical medium with absorbing boundary conditions. Using Gaussian input pulses, there was no enhanced nonlinear signal generation when comparing a composite to a uniform medium (this held for both types of boundary conditions). When using plane wave excitation, there was an enhancement for all periodic cases when compared to the uniform case, but only some composites generated enhancement when absorbing boundary conditions were used. For plane wave excitation, the change of the susceptibility for periodic and absorbing boundary conditions was strongly correlated (as one increased so did the other).

The enhancement for Raman nonlinearity depended on both the spacing between scatterers and the radius of the scatterers. Composites with low fill factors (~5%) using small scatterers ($a << \lambda$) showed the largest enhancement. Using very low fill factors (i.e. < 5%) gave smaller enhancements and did not alter the incoming pulse significantly (spatial profile similar, little time delay or pulse broadening). Large radius scatterers and/or using a high fill factor (~30%) reduced the effective susceptibility substantially and greatly altered the pulse profile.

Using a Kerr nonlinearity, there was a measured enhancement for many more cases than for a Raman nonlinearity. Again, it was noted that using low fill factors with small radius particles gave the largest enhancement. However, enhanced nonlinear signals could be generated using both Gaussian and plane wave excitation with either boundary condition.

Again, periodic boundary conditions enhanced the nonlinear signal over the absorbing boundary condition case. A final effect was noticed when using two input frequencies and looking at the mixing terms. For a Kerr nonlinearity, smaller scatterers generated higher frequencies more than larger scatterers (i.e. higher order mixing terms were generated preferentially than lower order ones). It is suspected that this behaviour is related to the frequency selective scattering observed in the linear case. It should trap certain frequencies for a longer period of time (preferential scattering), increasing the interaction length and further enhancing the signal.

## *5.3 Discussion of Results*

From the simulations, we see there are two main effects that have been neglected in the previous theoretical development. First, linear frequency dependent spatial effects play a role in determining the effective susceptibility of a nanocomposite. Second, using a medium of infinite extent to predict changes in susceptibility greatly overestimates the enhancement.

In [5] no frequency dependence is included and in [41] the frequency dependence of the material is included, but frequency dependent spatial effects are neglected. From our simulations, it has been observed that different frequencies are scattered unequally depending on particle size. Only in the case of very small scatterers (i.e. at least $<\lambda/20$) did this frequency dependent scattering become insignificant. Using the standard assumption that $a<<b<<\lambda$, we would expect this condition to be met. However, most experiments use nanoparticles (50-100nm in diameter) and visible or UV light, and this will not fulfil the condition for negligible spatial frequency effects. For experiments using two frequencies (i.e. CARS, SFG, etc.), this frequency dependence will most likely reduce the effective susceptibility since the two colours will have a shorter interaction length due to unequal scattering. This is likely part of the reason CARS generation generally showed less enhancement than nonlinear Kerr effect.

The most dramatic effect noticed was the role of diffraction and how including it changes the effective susceptibility. This is best illustrated by looking at CARS signal generation in a nonlinear medium with a low fill factor of small linear scatterers using plane wave excitation. When comparing a uniform medium (no scatterers, periodic boundary conditions) with a medium with scatterers and absorbing boundary conditions, we see a small enhancement towards the center and a reduction of signal towards the wings (see figure 30).

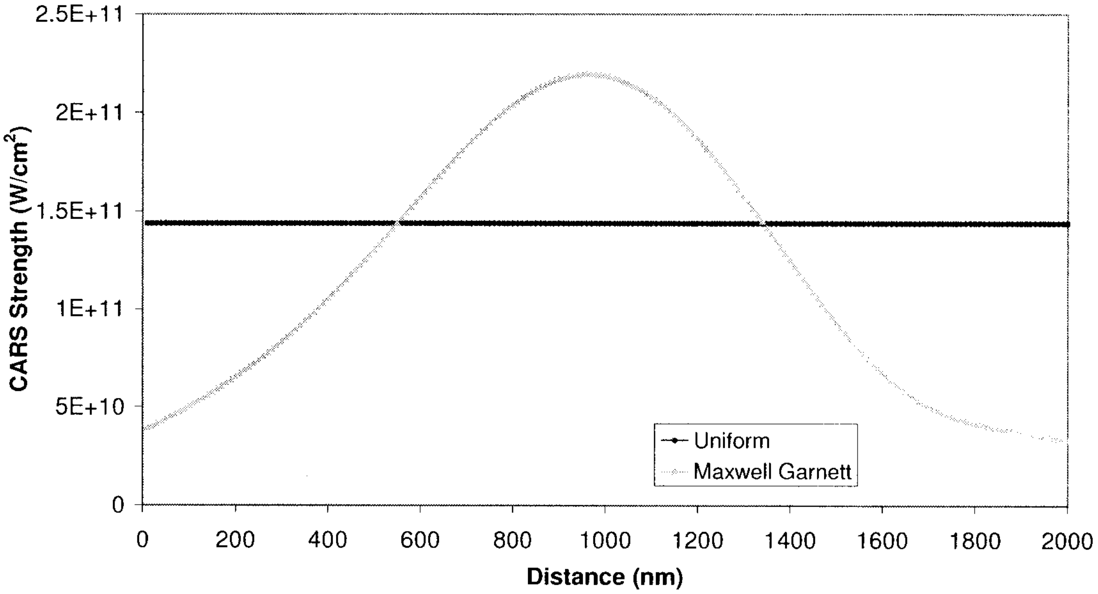

Figure 30. CARS signal generated from uniform medium and a medium with linear scatterers and absorbing boundary conditions.

Light from the edge of the medium is partially scattered out of the medium and partially towards the center. This is the main source of the enhancement seen in figure 30. It should be noted that the average nonlinear signal over the entire medium is lower with the scatterers than it is for a uniform medium. The enhancement in figure 30 is illustrative of the medium range local field enhancement due to multiple scattering discussed earlier. If the scattering light is prevented from escaping the medium, we would expect a large enhancement since the local field will be amplified in many places.

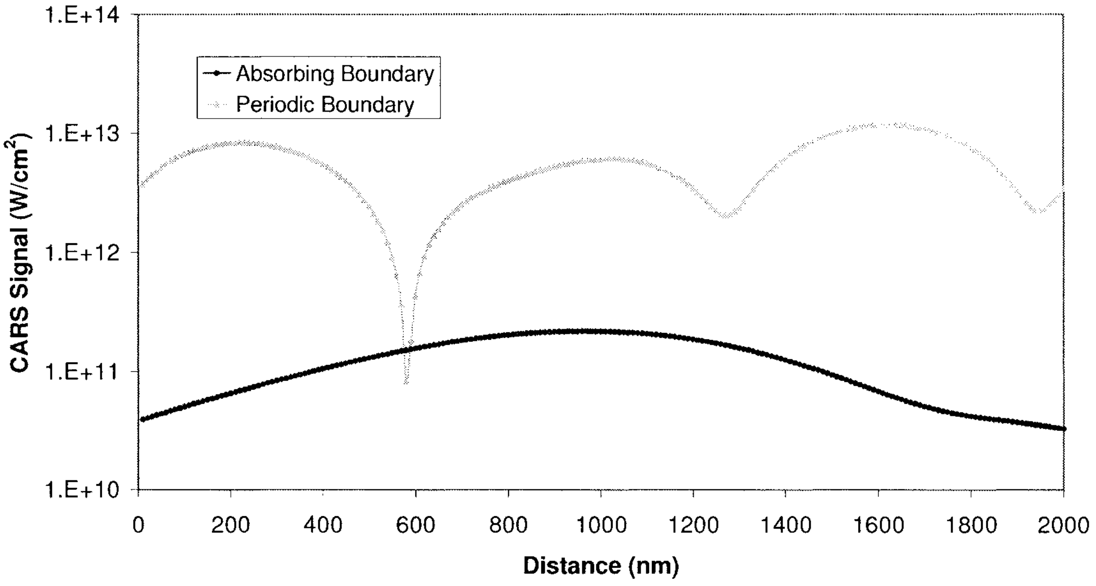

Figure 31. CARS signal generated from a nonlinear medium with linear scatterers using absorbing or periodic boundary conditions (N.B. logarithmic scale used).

From figure 31, we see that using periodic boundary conditions does in fact greatly enhance the signal (average signal is more than 50 times larger using periodic boundaries instead of absorbing ones). This illustrates a major deficiency in the current theoretical work. Experimentally, it would be difficult to generate periodic boundary conditions. They may be approximated by using a large beam spot size and measuring at the center, but as can be seen in figure 30, this where we expect the largest enhancement due to scattering and the enhancement does not exist across the entire medium.

As the medium becomes more densely packed, the diffraction effect becomes even larger. For densely distributed linear scatterers, there is only a reduction of the effective susceptibility when using absorbing boundary conditions. Even with the local field enhancements due to tight packing (see figure 27), the diffraction effect reduces the overall signal. If periodic boundary conditions are used with dense packing, the signal becomes very stochastic with some points experiencing a huge enhancement and others a reduction (see figure 29). This is due to the large variation of light direction and phase. Even with the large enhancement that is possible in this case, it is unlikely the signal would be of any practical use because of its random intensity, phase and propagation direction.

# 6 Conclusion

The field of nonlinear optics encompasses many fields and topics and has been the subject of continuous study since the invention of the laser. Two areas of recent interest have been nonlinear microscopy and the nonlinear optics of composite systems. Nonlinear microscopy is of great interest to the life sciences with its many benefits over traditional microscopy: better spatial resolution, longer excitation wavelength, chemical selectivity and low average power. Mesoscopic optics and nanocomposites open the possibility of designing devices the exhibit greatly enhanced nonlinear effects under user control.

With both nonlinear microscopy and nanocomposites design it is difficult to treat the full, complex system with analytical techniques. However, given the increase in computational power available to researchers over the past few years, it is now possible to address these topics using *ab initio* calculations. This gives us the possibility of developing new techniques and understanding of the processes involved.

One such numerical technique is the finite difference time domain (FDTD) method. This technique uses Maxwell's equations along with material models in order simulate real world systems. The model we developed is capable of modeling arbitrary systems with Raman and nonresonant electronic nonlinearities. Several different tests were performed and the model was found to agree very well with experimental and theoretical measurements. The one limitation of the model was an inability to model large spatial gradients in the electric field. However, for many systems, this is not an issue and, in principle, it may be avoided simply by using a smaller resolution.

The FDTD model was used to examine several real world problems. The first problem was to help explain anomalous measurements taken of myelinated nerve fibers. The fibers were found to emit a broadband signal in the epi (backward) direction. This signal did not resemble any known fluorescence or previously observed signals from such fibers. Given the spectral profile and spatial distribution of the signal, it was speculated that the thin myelin layer around the nerve axon had a large nonlinear susceptibility and that the generated signal was due to self-phase modulation. Using the FDTD model, we tested this assumption using a simple model of the nerve fiber. The predicted nonlinear signal from this simple model agreed with the previously measured signal. With the model as a guide, more measurements can now be taken in order to better understand this system.

Another type of nonlinear microscopy that can be studied with our model is coherent anti-Stokes Raman scattering (CARS) microscopy. This technique has shown great promise for both live cell and tissue imaging. However, for many desired applications, the current sensitivity and resolution must be improved. We have proposed a new technique which utilizes the coherent nature of the nonlinear signal generation in order to vastly improve the axial resolution of CARS microscopy. The phase of epi emitted nonlinear signals from subwavelength particles will depend on where in the focal volume the emitter is located. This phase information can be extracted using an interferometer, allowing us to follow particle movement in the axial direction with better than subwavelength resolution. Depending on the signal to noise ratio of the interferometric trace, it may be possible to achieve a resolution of 18 nm in real system, an improvement of 40 times over what current techniques achieve. This technique was tested using the FDTD model developed and found to agree very well with predictions. Although only CARS was tested with the FDTD model, using this interferometric technique should be able to improve the resolution of any nonlinear microscopy in which the signal is emitted in the epi direction.

The final system examined using the FDTD code developed was a Maxwell Garnett nanocomposite. This type of system is formed by placing spherical inclusions inside a host medium. This type of system has been previously examined under the assumption that the inclusions are small, widely spaced and exist in a medium of infinite extent. Under these assumptions, it has been predicted that the nonlinear susceptibility should be enhanced above that of either isolated constituent due to local field enhancements from scattering from the inclusions. This previous work has been confirmed in the limit of very widely spaced particles where the theory is best suited. However, using the FDTD model, it was shown that the predictions of the previous work fail when the medium becomes more densely packed. The two main reasons for this failure are linear frequency dependent spatial effects and diffraction. The problem of not treating particle-particle coupling in the previous theory was found to be a factor, but was insignificant compared to the other two previously overlooked effects. The linear frequency dependent scattering occurs when the inclusions are not sufficiently subwavelength (inclusions should be < λ/20). In this case, different frequencies are scattered by different amounts and in different directions. This greatly affects any predictions made for wave-mixing experiments but has less of an effect if dealing with monochromatic light (the predicted enhancement, however, should be frequency dependent). The larger effect is due to diffraction. Comparing simulations of mediums of infinite extent with those of only finite extent, it was found that the predicted enhancement was greatly overestimated. One reason this effect has not been previously observed is that it becomes more prominent as particle density increases. For very dense systems, there is a large reduction of the nonlinear susceptibility because of this effect, cancelling any enhancement due to particle-particle coupling. It should be noted that particle-particle enhancement is much larger with metallic inclusions instead of dielectric ones and that we only examined dielectrics inclusions.

By applying *ab initio* calculations to complex nonlinear optics problems, it is possible to reveal the processes at work and better understand the system. These techniques can be applied to many systems, including nonlinear microscopy and nanocomposites. This allows us to search for methods to enhance nonlinear effects while better understanding the limitations that are present.

# 7 References

1. Lagugne-Labarthet, F. and Y. R. Shen. "Nonlinear Optical Microscopy". in *Optical Imaging and Microscopy: Techniques and Advanced Systems.* edited by F. J. Kao and P. Torok, Springer Series in Optical Sciences vol. 87, Springer Verlag, 2003.

2. Yee, K. S. "Numerical Solution of Initial Boundary Value Problems Involving Maxwell's Equations in Isotropic Media" *IEEE Trans. Attenas and Propagation,* Vol. 14, pp. 302-307, 1966.

3. Sullivan, D. M. *Electromagnetic Simulation using the FDTD Method.* New York: IEEE Press, 2000.

4. Taflove, A. and S. C. Hagness. *Computational Electrodynamics: The Finite Difference Time Domain Method 2nd ed.* Boston: Artech House, 2000.

5. Sipe, J. E. and R. W. Boyd. "Nonlinear Susceptibility of Composite Optical Materials in the Maxwell Garnett Model" *Phys. Rev. A,* Vol. 46, pp. 1614-1629, 1992.

6. Fujii, M., M. Tahara, I. Sakagami, W. Freude, and P. Russel. "High-Order FDTD and Auxiliary Differential Equation Formulation of Optical Pulse Propagation in 2-D Kerr and Raman Nonlinear Dispersive Media" *IEEE J. Quantum Electron,* Vol. 40, pp. 175-181, 2004.

7. Gilles, L., S. C. Hagness, and L. Vazquez. "Comparison between Staggered and Unstaggered Finite Difference Time Domain Grids for Few-Cycle Temporal Optical Soliton Propagation" *J. Comp. Phys.,* Vol. 161 pp. 379-400, 2000.

8. Ziolkowski, R. W. "The Incorporation of Microscopic Material Models into the FDTD Approach for Ultrafast Optical Pulse Simulations" *IEEE Trans. Antennas and Propagation,* Vol. 45, pp. 375-391, 1997.

9. Agrawal, G. P. *Nonlinear Fiber Optics.* San Diego: Academic Press Inc., 1989.

10. Hellwarth, R. W. "Third Order Optical Susceptibilities of Liquid and Solids" *IEEE J. Prog. Quantum Electron,* Vol. 5, pp. 1-68, 1977.

11. Boyd, R. W., *Nonlinear Optics 2$^{nd}$ Edition,* San Diego: Academic Press Inc., 2003.

12. Flesch, R. G., A. Pushkarev, and J. V. Moloney "Carrier Wave Shocking of Femtosecond Optical Pulses" *Phys. Rev. Lett,* Vol. 76, pp. 2488 – 2491, 1996.

13. Richards, B. and E. Wolf "Electromagnetic Diffraction in Optical Systems II: Structure of the Image Field in an Aplanatic System" *Proc. R. Soc. London Ser. A,* Vol. 253, pp. 358 – 379, 1959.

14. Potma, E. O., X. S. Xie, L. Muntean, J. Preusser, D. Jones, J. Ye, S. R. Leone, W. D. Hinsberg, and W. Schade "Chemical Imaging of Photoresists with Coherent Anti-Stokes Raman Scattering (CARS) Microscopy" *J. Phys. Chem. B,* Vol. 108, pp. 1296 – 1301, 2004.

15. Cheng, J.-X., A. Volkmer, and X. S. Xie "Theoretical and Experimental Characterization of Coherent Anti-Stokes Raman Scattering Microscopy" *J. Opt. Soc. Am. B,* Vol. 19, pp. 1363 – 1375, 2002.

16. Cohen, L. B., R. D. Keynes and B. Hille "Light Scattering and Birefringence Changes During Nerve Activity" *Nature.* Vol. 218, pp. 438-441, 1968.

17. Maker, P. D. and R. W. Terhune, "Study of Optical Effects Due to an Induced Polarization Third Order in the Electric Field Strength" *Phys. Rev.* Vol. 137, pp. A801 – A818, 1965.

18. Duncan, M. D., J. Reintjes and T. J. Manuccia "Scanning Coherent Anti-Stokes Raman Microscope" *Opt. Lett.* Vol. 7, pp. 350 – 352, 1982.

19. Duncan, M. D., "Molecular Discrimination and Contrast Enhancement Using a Scanning Coherent Anti-Stokes Raman Microscope" *Opt. Commun,* Vol 50, pp. 307 – 312, 1984.

20. Zumbusch, A., G. R. Holtom and X. S. Xie, "Three Dimensional Vibrational Imaging by Coherent Anti-Stokes Raman Scattering" *Phys. Rev. Lett.* Vol. 82, pp. 4142 – 4145, 1999.

21. Volker, A., J.-X. Cheng, and X. S. Xie, "Vibrational Imaging with High Sensitivity via Epidetected Coherent Anti-Stokes Raman Scattering Microscopy" *Phys. Rev. Lett.* Vol. 87, pp. 023901-1 – 4, 2001.

22. Cheng, J.-X., L. D. Book, and X. S. Xie, "Polarization Coherent Anti-Stokes Raman Scattering Microscopy" *Opt. Lett.* Vol. 26 pp. 1341 – 1343, 2001.

23. Oron, D., N. Dudovich, D. Yelin and Y. Silberberg, "Narrow-Band Coherent Anti-Stokes Raman Signals from Broad-Band Pulses" *Phys. Rev. Lett.* Vol. 88, pp. 063004-1 – 4, 2002.

24. Oron, D. N. Dudovich, D. Yelin, and Y. Silberberg, "Quantum Control of Coherent Anti-Stokes Raman Processes" *Phys. Rev. A.* Vol. 65, pp. 043408-1 – 4, 2001.

25. Dudovich, N., D. Oron, and Y. Silberberg, "Single-Pulse Coherently Controlled Nonlinear Raman Spectroscopy and Microscopy" *Nature.* Vol. 418, pp. 512 – 514, 2002.

26. Volkmer, A., L. D. Book, and X. S. Xie, "Time-Resolved Coherent Anti-Stokes Raman Scattering Microscopy: Imaging based on Raman Free Induction Decay" *Appl. Phys. Lett.* Vol. 87, pp. 1505 – 1507, 2002.

27. Schaller, R. D., J. Ziegblbauer, L. F. Lee, L. H. Haber, and R. J. Saykally, "Chemical Selective Imaging of Subcellular Structure in Human Hepatocytes with Coherent Anti-Stokes Raman Scattering (CARS) Near-Field Scanning Optical Microscopy (NSOM)" *J. Phys. Chem. B.* Vol. 106, pp. 8489 – 8492, 2002.

28. Ichimura, I., N. Hayazawa, M. Hashimoto, Y. Inouye, and S. Kawata, "Tip-Enhanced Coherent Anti-Stokes Raman Scattering for Vibrational Nanoimaging" *Phys. Rev. Lett.* Vol. 92, pp. 220801-1 – 4, 2004.

29. Vinegoni, C, J. S. Bredfeldt, D. L. Marks and S. A. Boppart, "Nonlinear optical contrast enhancement for optical coherence tomography" *Opt. Exp.* Vol. 12, pp. 331 – 341, 2004.

30. Cheng, J.-X., and X. S. Xie, "Coherent Anti-Stokes Raman Scattering Microscopy: Instrumentation, Theory and Applications" *J. Phys. Chem. B.* Vol. 108, pp. 827 – 840, 2004.

31. Hochmuth, R. M., C. A. Evans, H. C. Wiles, and J. T. McCown, "Mechanical Measurements of Red Cell Membrane Thickness" *Science.* Vol. 220, pp. 101 – 102, 1983.

32. Bruggeman, D. A. G. "Berechnung Verschiederner Physikalischer Konstantne von Heterogenen Substanzen. I. Dielektrizitatskonstatnetn und Leitfahigkeiten der Miscchkorper aus Isotropen Substanzen" *Ann. Phys.* Vol. 24 pg. 636, 1935. [Reproduced in Lakhtakia, A. (Ed.), *Selected Papers on Linear Optical Composite Materials.* Bellingham, WA, USA: SPIE, 1996.]

33. Maxwell Garnett, J. C. “Colours in Metal Glasses and in Metallic Films” *Phil. Trans. R. Soc. A.* Vol. 203, pp. 385 – 420, 1904.

34. Canham, L. T., “Si Quantum Wire Array Fabrication by Electrochemical and Chemical Dissolution” *Appl. Phys. Lett.* Vol. 57, pp. 1046-1048, 1990.

35. Lehmann, V. and U. Gosele, ”Porous Silicon Formation: Quantum Wire Effect” *Appl. Phys. Lett.* Vol. 58, pp. 856 – 858, 1991.

36. Fisher, G. L., R. W. Boyd, R. J. Gehr, S. A. Jenekhe, J. A. Osaheni, J. E. Sipe, and L. A. Weller-Brophy, “Enhanced Nonlinear Optical Response of Composite Materials” *Phys. Rev. Lett.* Vol. 74, pp. 1871 – 1874, 1995.

37. Boyd, R. W. and J. E. Sipe, “Nonlinear Optical Susceptibilities of Layered Composite Materials” *J. Opt. Soc. Am. B.* Vol. 11, pp. 297 – 303, 1994.

38. Nelson, R. L. and R. W. Boyd, “Enhanced Eletro-Optic Response of Layered Composite Materials” *App. Phys. Lett.* Vol. 74, pp. 2417 – 2419, 1999.

39. Bloembergen, N., *Nonlinear Optics,* New York: Benjamin, 1965.

40. Pellegrini, Y.-P., “Self Consistent Effective-Medium Approach for Strongly Nonlinear Media” *Phys. Rev. B.* Vol. 64, pp. 134211-1 – 11, 2001.

41. Stockman, M. I. and K. B. Kurlayev, “Linear and Nonlinear Optical Susceptibilities of Maxwell Garnett Composites: Dipolar Spectral Theory” *Phys. Rev. B.* Vol. 60, pp. 17071 – 17083, 1999.

42. Ma, H., R. Xiao and P. Sheng, “Third-Order Optical Nonlinearity Enhancement through Composite Microstructures” *J. Opt. Soc. Am. B.* Vol. 15, pp. 1022 – 1029, 1998.

43. Smith, D. D., G. Fisher, R. W. Boyd, and D. A. Gregory, “Cancellation of Photoinduced Absorption in Metal Nanoparticle Composites through a Counterintuitive Consequence of Local Field Effect” *J. Opt. Soc. Am. B.* Vol. 14, pp. 1625 – 1631, 1997.

44. Jackson, J. D., *Classical Electordynamics*, Toronto: John Wiley & Sons, 1962.

45. Shalaev, V. M. “Electromagnetic Properties of Small-Particle Composites” *Phys. Rep.* Vol. 272, pp. 61 – 137, 1996.

46. Shalaev, V. M., M. I. Stockman and R. W. Boyd, "Resonant Excitations and Nonlinear Optics of Fractals" *Physica A.* Vol. 185, pp. 181-186, 1992.

47. Stockman, M. I., L. N. Pandey, L. S. Muratov and T. F. George, "Giant Fluctuations of Local Optical Fields in Fractal Clusters" *Phys. Rev. Lett.* Vol. 72, pp. 2486 – 2489, 1994.